

Transient fluid-combustion phenomena in a model scramjet

S. J. Laurence[†], S. Karl, J. Martinez Schramm and K. Hannemann

Institute of Aerodynamics and Flow Technology, Spacecraft Department, German Aerospace Center,
Bunsenstr a e 10, 37073 G ottingen, Germany

(Received 9 February 2012; revised 19 October 2012; accepted 22 January 2013;
first published online 28 March 2013)

An experimental and numerical investigation of the unsteady phenomena induced in a hydrogen-fuelled scramjet combustor under high-equivalence-ratio conditions is carried out, focusing on the processes leading up to unstart. The configuration for the study is the fuelled flow path of the HyShot II flight experiment. Experiments are performed in the HEG reflected-shock wind tunnel, and results are compared with those obtained from unsteady numerical simulations. High-speed schlieren and OH* chemiluminescence visualization, together with time-resolved surface pressure measurements, allow links to be drawn between the experimentally observed flow and combustion features. The transient flow structures signalling the onset of unstart are observed to take the form of an upstream-propagating shock train. Both the speed of propagation and the downstream location at which the shock train originates depend strongly on the equivalence ratio. The physical nature of the incipient shock system, however, appears to be similar for different equivalence ratios. Both experiments and computations indicate that the primary mechanism responsible for the transient behaviour is thermal choking, though localized boundary-layer separation is observed to accompany the shock system as it moves upstream. In the numerical simulations, the global choking behaviour is dictated by the limited region of maximum heat release around the shear layer between the injected hydrogen and the incoming air flow. This leads to the idea of ‘local’ thermal choking and results in a lower choking limit than is predicted by a simple integral analysis. Such localized choking makes it possible for new quasi-steady flow topologies to arise, and these are observed in both experiments and simulation. Finally, a quasi-unsteady one-dimensional analytical model is proposed to explain elements of the shock-propagation behaviour.

Key words: combustion, gas dynamics, shock waves

1. Introduction

Transient phenomena in scramjet engines are associated with such critical operational processes as dual-mode scramjet/ramjet transition and the onset of inlet unstart. The issue of unstart is a particularly important one. Defined as the upstream displacement or ‘disgorging’ of the original inlet shock system (Heiser & Pratt 1994), unstart can cause violent and unsteady thermal and aerodynamic loads, even leading to the destruction of the engine; witness the recent failure of the second X-51 flight

[†] Email address for correspondence: stuart.laurence@dlr.de

experiment (Musielak 2011). The causes of inlet unstart can be divided broadly into two groups: aerodynamic phenomena associated with the inlet flow itself, such as changes in Mach number or angle of attack, or boundary-layer separation on an intake surface; and processes that originate downstream in the combustion chamber of the engine. The latter, involving complex interactions between flow and combustion features, are challenging to study and form the focus of the present investigation. Thus, the term ‘unstart’ is to be understood hereinafter as referring to the process whereby abnormal operating conditions in the combustion chamber generate upstream-propagating disturbances that subsequently affect the inlet flow.

Incipient unstart in scramjet engines is typically brought about through one of two processes, or a combination thereof. In the first, excessive heat release in the combustion chamber results in the reduction of the flow Mach number to sonic conditions. A Rayleigh-flow analysis shows that there is no steady solution for further heat addition beyond this sonic point; therefore, the flow responds by sending pressure disturbances upstream to modify the inlet flow. This unstart mechanism is referred to as thermal choking. In the second process, the combustion-induced adverse pressure gradient causes the wall boundary layer(s) to separate, resulting in the formation of an oblique shock train, which then propagates upstream. In the dual-mode ramjet/scramjet concept, this oblique shock train (or the normal shock train produced by thermal choking) may be stabilized in the isolator ahead of the combustor, but if the combustion-related pressure rise is too great, the shock train will continue moving upstream and unstart the inlet (Curran, Heiser & Pratt 1996).

The transient flow phenomena associated with the onset of unstart have been the subject of a number of experimental investigations. In most of these, the combustion-induced pressure rise is replaced with mechanical throttling of the flow, for example, by pins (Wieting 1976), deflecting flaps (Rodi, Emami & Trexler 1996; Wagner *et al.* 2009) or plugs (Tan & Guo 2007; Tan *et al.* 2011), or through mass addition (Do *et al.* 2011). This allows the use of cold flows and the simpler implementation of diagnostic techniques. These studies have yielded information regarding unstart shock systems in isolators and inlets and the unsteady flow oscillations produced once full inlet unstart conditions are reached. Such an approach, however, is inadequate for gaining understanding of the interacting combustion–flow phenomena leading up to unstart in the combustion chamber itself.

In other studies, unstart has been induced by the injection of hydrogen at high equivalence ratios in model scramjet combustors. Shimura *et al.* (1998) carried out experiments on a large-scale scramjet engine attached to a force measurement system. As the equivalence ratio was increased, pressure spikes were observed to develop with a frequency that increased with the strength of the subsequent unstart. Once unstart was established, violent oscillations in both the measured wall pressure and thrust were observed. The formation of an upstream-propagating separation bubble was postulated as the source of the pressure spikes, but the limited diagnostics employed meant that no further conclusions could be drawn. A study of a more fundamental nature was carried out by O’Byrne *et al.* (2000) in the T3 reflected-shock wind tunnel. Single-frame shadowgraphy and time-resolved pressure measurements were employed to investigate the thermal choking behaviour in a simple combustor, but again only limited information could be derived regarding the interaction between the combustion phenomena and the observed flow features. An additional source of uncertainty in these experiments was the high degree of driver-gas contamination often present during the choking process.

Computational fluid dynamics (CFD) simulations potentially provide a valuable counterpart to experimental unstart investigations, as they afford a detailed picture of the three-dimensional combusting flow field. However, the chemically reacting nature of the flow, the uncertainty in turbulence models, and the strongly interacting viscous–inviscid flow features make even steady computations challenging. For time-resolved unsteady simulations, computational cost becomes a further issue. The difficulty of obtaining acceptable agreement between unsteady computations and experiments was demonstrated by the work of McDaniel & Edwards (1999, 2001), who carried out both two- and three-dimensional simulations of experiments performed in the Vitiated Air Generator (VAG) of the Japanese National Aerospace Laboratory (Boyce *et al.* 2000) at two fuelled equivalence ratios, ϕ . At the higher equivalence ratio ($\phi = 0.61$), experimental choking was observed; consistent transient behaviour developed in the simulations, with massive combustion-induced separation leading to rapid unstart. At the lower value ($\phi = 0.29$), however, three-dimensional simulations showed a slow progression to unstart, in contrast to the stable combustion observed in both experiments and two-dimensional simulations. Questions remained concerning the grid resolution, the combustion model and the choice of boundary conditions. Unsteady CFD simulations were also carried out by Sunami & Kodera (2012), in an attempt to reproduce the transient behaviour observed in experiments on the HyShot IV hypermixer scramjet (Sunami *et al.* 2006) at equivalence ratios of unity or above. Qualitative agreement was obtained, with the development of a strong moving pressure front in both experiments and simulations, which was identified as a detonation wave. The computational boundary conditions had to be artificially modified in order to achieve ignition, however, and a large discrepancy was observed between experimental and numerical wave speeds.

In the present study, the transient flow and combustion features induced by the injection of hydrogen at high equivalence ratios in a scramjet combustor are investigated experimentally in a wind-tunnel reproduction of the HyShot II flight configuration. The diagnostic tools employed – time-resolved surface pressure measurements, and high-speed schlieren and OH* chemiluminescence visualization – allow an unprecedented level of insight into the interacting fluid and combustion phenomena. Unsteady numerical simulations are employed alongside the experiments to provide detailed information concerning the mechanisms responsible for the transient behaviour. The layout of this paper is as follows. The experimental and numerical methodologies are described in §§ 2 and 3. A brief discussion of stable combustion results appears in § 4, and in § 5 experimental and computational results pertaining to the unsteady phenomena leading up to unstart are presented. In § 6, we describe experimental measurements made under full unstart conditions. A discussion of the salient points follows in § 7, and a simple one-dimensional quasi-unsteady model is proposed in § 8 to explain elements of the observed transient behaviour. Conclusions are drawn in § 9.

2. Experimental methodology

2.1. Facility and test conditions

All experiments were carried out in the High Enthalpy shock tunnel Göttingen (HEG) facility of the German Aerospace Center (DLR). The HEG is a reflected-shock wind tunnel, capable of producing flows over a wide range of stagnation pressures and total enthalpies. Further information on the operating principles and the test conditions achievable in HEG is provided in Hannemann (2003). Briefly, to initiate a test run,

	Reservoir		Free stream				
	p_0 (MPa)	h_0 (MJ kg ⁻¹)	p (kPa)	ρ (kg m ⁻³)	T (K)	u (m s ⁻¹)	M
Mean	16.7	3.14	2.00	0.0263	264	2390	7.32
±	0.8	0.12	0.10	0.0013	8	50	0.02

TABLE 1. Mean facility reservoir and free stream conditions from the present experiments, together with estimated single-shot uncertainties.

compressed air is used to accelerate a free piston down a compression tube filled with a mixture of helium and argon. A primary diaphragm initially separates the compression tube from the shock tube containing the test gas, in this case air. When the pressure in front of the piston reaches a sufficiently high level, the diaphragm bursts, sending a strong shock wave down the shock tube. This shock reflects from the far end of the shock tube, rupturing the secondary (mylar) diaphragm, which until this instant separates the evacuated tunnel nozzle and test section from the shock tube. The reflected shock decelerates the test gas in the shock tube to stagnation conditions, forming a reservoir for the subsequent expansion through the hypersonic nozzle and into the test section. Quasi-steady test conditions typically persist for several milliseconds; the test time is terminated either by the arrival of the expansion wave from the primary diaphragm burst or by contamination of the test flow by the driver (compression tube) gas.

For all tests in the current investigation, we employed HEG condition XIII, designed to simulate the flight conditions of the HyShot II vehicle at 28 km altitude. The mean stagnation pressure and enthalpy from the present sequence of experiments are provided in table 1, together with estimated single-shot uncertainties. The pressure is measured directly using redundant sensors; the quoted 5% uncertainty value incorporates both temporal variation and errors in the transducer calibrations. The enthalpy is calculated from the pressure and measured shock speed using a standard method (Krek & Jacobs 1993); the associated uncertainty is derived assuming an accuracy in the shock-speed measurement of 3%. The shot-to-shot variation was of the same order as the single-shot uncertainty: 95% confidence values of 0.8 MPa and 0.09 MJ kg⁻¹ were obtained over the entire experimental campaign.

Also provided in table 1 are free stream conditions at the model intake derived from a CFD simulation employing the mean reservoir conditions. In HEG, we compare such nozzle computations with extensive calibration-rake measurements; factors such as the chemistry modelling and boundary-layer transition location are adjusted to provide the closest fit to the calibration data. For the present low-enthalpy case, the excellent agreement between calibration measurements and the tuned simulation results (see Hannemann *et al.* 2010) makes it reasonable to assume that the additional error contributions from the simulation are negligible. Thus, the free stream uncertainties in table 1 correspond solely to propagated values from the single-shot reservoir uncertainties. The corresponding shot-to-shot variations can be derived in a similar manner.

In figure 1 we plot reservoir, Pitot and static pressure measurements (the latter two scaled to allow a direct comparison) from a typical experiment in the present study. The point $t = 0$ corresponds to the instant of shock reflection from the shock-tube endwall, a convention used throughout this paper. The time scale of the reservoir trace has been shifted to account for the passage of the flow through the nozzle. The

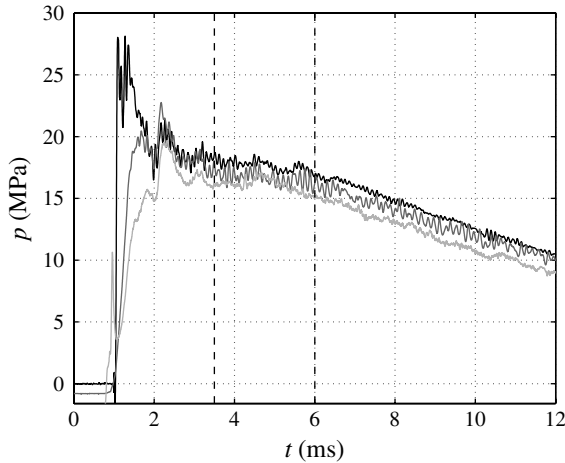


FIGURE 1. Typical measured reservoir (dark), free stream Pitot (medium) and free stream static (light) pressure traces for the test condition used in the present experiments. The time scale of the reservoir trace has been shifted to account for the passage of the flow through the nozzle, and the free stream traces have been vertically scaled and shifted to allow convenient comparison. The quasi-steady test time is indicated by vertical dashed lines.

quasi-steady test time, from 3.5 to 6.0 ms, is indicated by dashed vertical lines. This was the typical test duration chosen for steady combustion experiments; nevertheless, the flow is established and has achieved roughly constant conditions by 2.5 ms. This latter point will be important in the results discussed in § 5, as the transient phenomena under investigation here were usually initiated before the beginning of the nominal test period.

Previous investigations (Hannemann *et al.* 2000) have shown that a comparison of the static pressure development with that of the reservoir and Pitot pressures gives a good indication of the onset of driver-gas contamination: the Pitot pressure is typically unaffected by the arrival of driver gas in the free stream and continues to follow the reservoir pressure, but the static pressure drops more rapidly once driver gas is present. In figure 1, we note that the static pressure development follows that of the reservoir and Pitot pressures until at least 12 ms, indicating that there is no significant contamination during this time. The steady test time is instead terminated by the arrival of the expansion wave from the primary-diaphragm burst.

2.2. Model configuration

The experimental model used in this investigation was a 1 : 1 scale reproduction of the fuelled flow path of the HyShot II flight experiment (Paull, Alesi & Anderson 2003; Smart, Hass & Paull 2006). HyShot II was the first successful flight in the HyShot programme of the University of Queensland, designed to provide benchmark supersonic combustion data at a flight Mach number of approximately $M = 8$. Extensive ground testing of the HyShot II configuration has already been carried out, both at the University of Queensland (Smart *et al.* 2006; Frost *et al.* 2009) and in HEG (Gardner *et al.* 2004; Hannemann *et al.* 2008, 2010), and its simple combustion-chamber design, allowing for convenient optical access, made it suitable for the present study. The basic model configuration was as tested in the previous

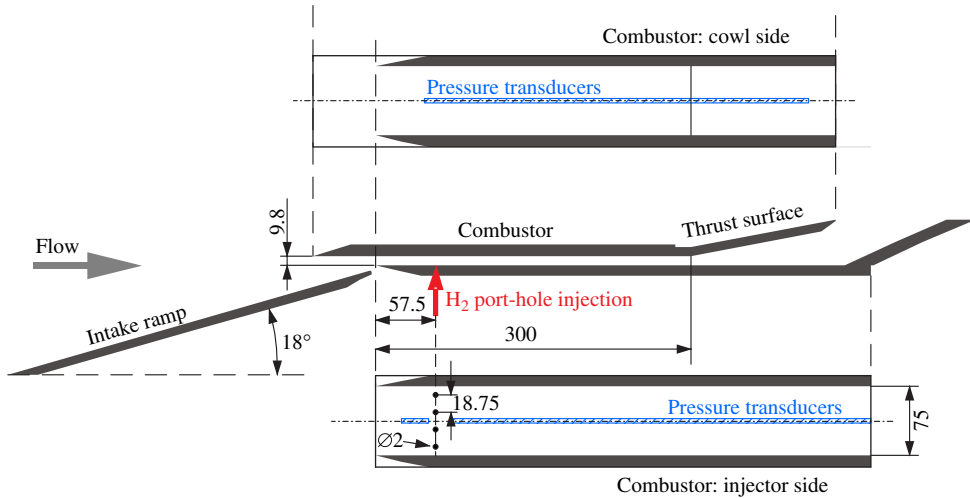


FIGURE 2. (Colour online) Schematic drawing of the HyShot II model flow path; all dimensions are in millimetres. The origin of the x -coordinate system used throughout this work is the leading edge of the injector-side wall.

HEG experiments just referred to, with modifications to improve handling and optical access.

A schematic of the model flow path is presented in figure 2. The intake is a simple wedge of half-angle 18° ; the use of sidewalls, together with the increased width of the intake ramp in comparison to that of the combustion chamber (196 versus 75 mm), ensured the two-dimensionality of the flow at the combustion chamber entrance. To prevent the intake-ramp boundary layer from entering the combustion chamber, a bleed channel is situated between the intake and the combustor entrance. This channel also serves to swallow the shock generated at the leading edge of the cowl. The combustion chamber is a constant-area rectangular duct of 300 mm length and 75 mm \times 9.8 mm cross-section, and is followed by a simple two-dimensional expansion formed by two exhaust-surface plates. To allow visualization of the flow and combustion features, windows were installed on either side of the combustion chamber, extending from 2 mm upstream of the injection location into the exhaust region. For all experiments described herein, the model was mounted at an angle of attack of 3.6° , i.e. the intake ramp formed an angle of 21.6° to the free stream. The average flow conditions at the entrance to the combustor were computed as $M = 2.49 \pm 0.01$, $T = 1370 \pm 40$ K, $p = 127 \pm 6$ kPa and $\rho = 0.317 \pm 0.016$ kg m $^{-3}$ (see § 3). The single-shot uncertainties quoted here are based on those for the free stream conditions provided in table 1, including an additional 0.1° uncertainty in the angle of attack.

Hydrogen fuel was injected in the wall-normal direction through four evenly spaced port-holes on the intake-ramp-side wall of the combustion chamber (hereinafter referred to as the injector-side wall) at a distance 58 mm downstream from the wall leading edge. The injection port-holes were each of radius 1 mm, providing a total injection area of 12.6 mm 2 . The hydrogen was supplied via a Ludwieg tube, capable of providing an approximately constant pulse of fuel for 50 ms. To ensure the hydrogen flow was fully established by the arrival of the test gas, injection was

initiated by opening a fast-acting solenoid valve ~ 20 ms before the test time. The hydrogen mass flux was calculated for each shot from the measured plenum pressure, using an effective injection cross-sectional area derived from CFD simulations of the injector. Assuming a 5% uncertainty in the injection mass flux, the single-shot uncertainty in the equivalence ratio is approximately 8%.

2.3. Measurement techniques

The model was heavily instrumented with both pressure transducers and thermocouples for heat-flux measurements, though the latter will not be discussed in the present work. In total, 57 pressure transducers were distributed over the inlet ramp, the combustion chamber walls and the exhaust surfaces. The model was also equipped with probes to measure the free stream Pitot and static pressures. In the combustion chamber, a single row of pressure transducers was installed on each of the injector and cowl-side walls along the model plane of symmetry, as shown in figure 2. The transducer type was the Kulite XCEL-100, with a pressure range, depending on the particular transducer, of between 170 and 700 kPa and a resonant frequency above 150 kHz. The uncertainty in the model pressure measurements is estimated as 5%.

Flow structures within the combustion chamber were visualized using high-speed schlieren imaging. The light source was a Cavilux Smart 690 nm pulsed diode laser. The short pulse duration employed (30 ns) effectively froze the visualized flow structures, while the use of monochromatic light allowed extraneous luminosity to be removed with a bandpass filter. An additional advantage of this device is that the beam is effectively incoherent, eliminating the diffraction effects usually associated with laser light sources (Settles 2006). A conventional Z-fold schlieren set-up with a horizontal knife edge was employed, with images recorded by a Shimadzu HPV-1 camera. Typical frame rates were 16 000 or 32 000 frames per second. The limited pixel count of the Shimadzu camera (312×260 pixels) meant that, in order to provide acceptable resolution across the duct height, only approximately one-third of the visible duct length was visualized in a given experiment.

Additionally, the approximate flame location in the combustion chamber was determined through OH^* chemiluminescence visualization. OH^* chemiluminescence intensity, being a line-of-sight quantity, is limited in its ability to provide quantitative results when measured in three-dimensional flow fields. Nevertheless, it gives a reliable indication of the global onset of combustion and has been recommended as an attractive option even for more complex hydrocarbon flames where other, especially laser-based, techniques would be difficult to apply (Haber & Vandsburger 2003). It is also suitable for the high frame rates necessary to investigate the unsteady phenomena that are of interest in the present study. The OH^* visualization apparatus consisted of the Shimadzu HPV-1 high-speed camera together with a LaVision HS-IRO intensifier. Since only a single high-speed camera was available, OH^* and schlieren images could not be obtained simultaneously. For the OH^* visualization experiments, both the model combustor sidewall and the HEG test section were fitted with quartz windows to allow transmittance of the relevant wavelengths. A custom bandpass filter of 50 nm width centred at 310 nm was placed in front of the intensifier, reducing both other flame emissions and the self-luminosity associated with the facility to negligible levels. For steady combustion tests ($\phi = 0.33$), images were captured at 8000 frames per second, with an integration time of 60 μs , whereas for higher equivalence ratios, the more intense combustion allowed a shorter exposure time of 10 μs combined with a camera frame rate of 16 000 frames per second.

3. Computational methodology

3.1. Numerical model

All numerical simulations in the present study were performed with the hybrid structured–unstructured DLR Navier–Stokes solver TAU (Gerhold *et al.* 1997). The TAU code is a second-order finite-volume flow solver for the Euler and Navier–Stokes equations in their integral forms, using eddy viscosity, Reynolds stress or detached and large eddy simulation for turbulence modelling. For the present investigation, we employed the Spalart–Allmaras one-equation eddy viscosity model. The AUSMDV flux-vector splitting scheme was applied together with MUSCL gradient reconstruction to achieve second-order spatial accuracy. In unsteady computations, the dual time-stepping technique described by Jameson (1991) was used.

The combustion model in the TAU code is an extension of the chemical and thermal non-equilibrium models used to simulate high-enthalpy re-entry flows. The fluid is considered to be a reacting mixture of thermally perfect gases, with a transport equation solved for each of the individual species. The chemical source terms in this set of transport equations are computed from the law of mass action by summation over all participating reactions. The forward reaction rate is computed using the modified Arrhenius law, and the backward rate is obtained from the equilibrium constant, which is derived directly from the partition functions of the participating species. A modified Jachimowski reaction mechanism for hydrogen–air mixtures, as described by Gerlinger (2001), was applied for this investigation. This mechanism includes both hydrogen peroxide (H_2O_2) and the perhydroxyl radical (HO_2) and has been shown to be applicable over a wide range of pressures, densities and equivalence ratios. Validation of the combustion model implemented in TAU can be found in Karl (2011).

The thermodynamic properties (energy, entropy, specific heat) are calculated using the partition functions for each individual species in the reacting gas mixture. Knowledge of the mixture composition and the thermodynamic state of the individual species allows the properties of the reacting gas mixture to be computed using suitable mixture rules, such as those proposed by Wilke (1950) for viscosity and by Hering & Zipperer (1936) for heat conductivity. A non-catalytic wall boundary condition, i.e. a von Neumann condition, is used for the species partial densities. The species diffusion fluxes are modelled using Fick's law, applying an averaged diffusion coefficient for all species. The approximate diffusion coefficient thus derived is computed using the laminar and eddy viscosities, and constant Schmidt numbers (laminar and turbulent) of 0.7. Dedicated modelling of turbulence–chemistry interactions is neglected in this study.

3.2. Computational domains and boundary conditions

The CFD analysis of the HyShot II configuration was split into a two-dimensional simulation of the intake flow and a three-dimensional analysis of the combustor flow. Simulation of the entire combustor would result in a prohibitive computational cost; thus, the symmetries of the geometry were exploited and only a slice covering one-eighth of the physical domain was considered, with symmetry conditions applied at the spanwise boundaries. The free stream conditions for the intake computation were assumed to be constant in space and were obtained by averaging the results of an HEG nozzle-flow simulation employing the approximate reservoir conditions used in the present study. Karl & Hannemann (2008) and Hannemann *et al.* (2010) provide further details of this methodology.

For the combustor section, the flow profile obtained from the intake analysis was prescribed as a Dirichlet boundary condition at the inflow plane located 5 mm downstream from the leading edge of the injector-side wall. The outflow plane was located at $x = 410$ mm, i.e. 110 mm of the exhaust expansion were included. The boundary condition applied at this plane was an upwind-flux-based pressure outlet, consisting of a simple extrapolation of the conservative variables in the supersonic flow region and a prescription of the exit pressure (i.e. the test-section back-pressure) in subsonic flow regions. Symmetry boundary conditions were applied at the spanwise boundary planes: one located along a cut through the centre of an injection port-hole, the other on the plane midway between two port-holes. The bottom and top walls were modelled with a viscous no-slip boundary condition, for which the wall temperature was fixed at 300 K to account for the short test time in HEG. Transition from laminar to turbulent flow in the wall boundary layers was set according to a criterion based on Re_θ , the momentum-thickness Reynolds number, as $Re_\theta/M_e = 200$, where M_e is the Mach number at the boundary-layer edge (Bertin *et al.* 1997). The suitability of this criterion was supported by surface heat-flux measurements inside the combustor.

The hydrogen injection was modelled by partially including the injector in the computational domain. A reservoir inflow condition was applied at the hydrogen inflow boundary: the thermodynamic conditions were computed using an isentropic expansion from prescribed stagnation conditions using the inflow velocity vector, obtained as part of the CFD solution. The computational grid covering the combustor domain consisted of approximately one million cells. Structured prismatic sublayers were used at the viscous walls; a dimensionless wall spacing of $y^+ = O(1)$ ensured sufficient resolution for the low-Reynolds-number turbulence model and for computation of the wall heat flux. Further information regarding the computational methodology can be found in Karl (2011).

4. Stable combustion

In order to provide a context for the unsteady combustion results discussed in the following section, we begin by briefly outlining results from experiments and computations in which steady combustion was established within the combustor.

4.1. Experimental results

Stable combustion was obtained in experiments by limiting the equivalence ratio to around 0.33. In figure 3 we show the static pressure distribution along the injector-side wall, averaged over the test time, in one such experiment; this is compared with an equivalent fuel-off distribution. The error bars in each case indicate the time-varying standard deviation in pressure during the test time. Within the constant-area section of the combustor ($x = 0\text{--}300$ mm), a gradual rise in the pressure level (as indicated by the dashed trend line) is clearly visible in the fuel-on profile, in contrast to the approximately constant pressure for the fuel-off case. The fuel-on profile, lacking the characteristic pressure plateaus typically associated with boundary-layer separation in a constant-area duct (Curran *et al.* 1996), is indicative of ‘clean’ supersonic combustion. There are significant fluctuations superimposed upon the general upward trend: these are produced by reflections of the injection-generated shock propagating down the duct, which generates sharp variations in the local pressure. The positions of these reflected shocks are slightly unsteady, which leads to larger variations in pressure at locations close to the reflection points (these can be identified by the local peaks in figure 3). In comparison, the error bars for the fuel-off experiment are generally closer

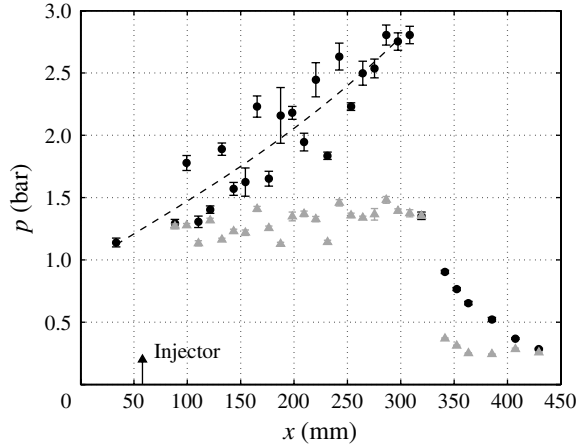


FIGURE 3. Mean pressure profiles on the injector-side wall of the HyShot II combustor for fuel-off conditions (\blacktriangle) and for an equivalence ratio of 0.33 (\bullet). The dashed line indicates the fuel-on trend within the constant-area section of the combustion chamber ($x = 0\text{--}300$ mm).

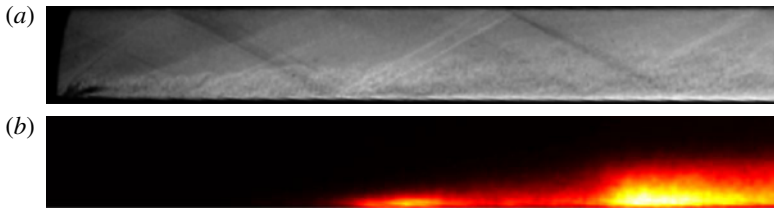


FIGURE 4. (Colour online) (a) Schlieren and (b) OH^* chemiluminescence visualizations of the flow downstream of the injector ($x = 56\text{--}136$ mm) for an equivalence ratio of 0.33.

to one another in magnitude. In the diverging section of the geometry ($x > 300$ mm), a steep drop in static pressure is observed.

In figure 4 are shown schlieren and OH^* chemiluminescence visualizations of the section of the combustion chamber immediately downstream of injection (56–136 mm). The point of injection is at the lower left corner of each image. To improve the signal-to-noise ratio, the OH^* image has been averaged over 17 visualizations recorded during the steady test time of a single experiment. The barrel shock generated by the hydrogen injection is clearly visible in the schlieren image, together with several of its reflections extending down the duct. The freezing of the turbulent structures in the hydrogen jet, enabled by the short pulse duration of the light source, is also shown to good effect here. The injected hydrogen has penetrated to approximately half the duct height by the downstream end of the visualized section. The OH^* visualization shows the onset of combustion to be clearly linked to the shock structure in the duct: namely, the first reflection of the injection shock appears to initiate combustion close to the injector-side wall; the second reflection then ‘kicks’ the flame further out into the duct and increases the intensity of combustion.

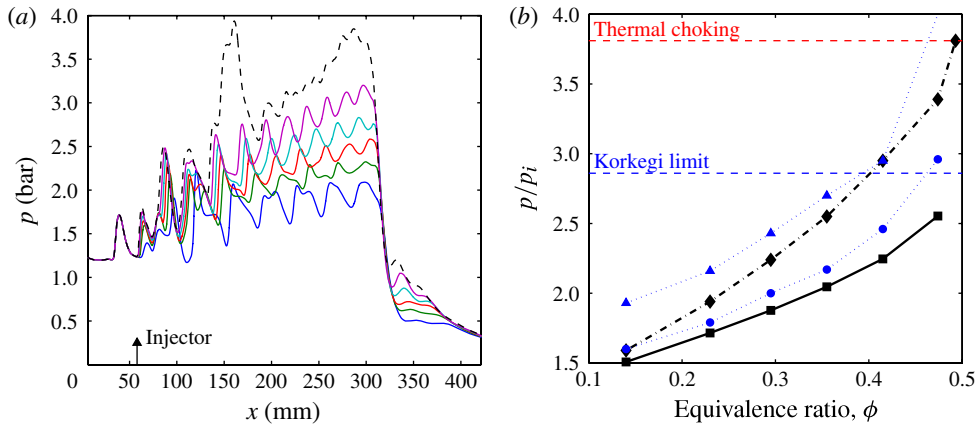


FIGURE 5. (Colour online) (a) Computed surface pressure distributions on the injector-side wall for equivalence ratios of (solid lines, minimum to maximum levels) 0.140, 0.230, 0.295, 0.355 and 0.415, and (dashed) 0.474. (b) Combustor pressure ratios obtained from stream-thrust averaging the computational results (■) and an equilibrium control-volume analysis (◆), together with maximum computed pressures on both the injector side (●) and cowl side (▲) walls, all as functions of the computational equivalence ratio. Also shown are the estimated critical pressure ratios for thermal choking and boundary-layer separation.

4.2. Analysis of operational limits

In order to investigate the response of the HyShot II combustor to variations in the equivalence ratio, and, in particular, to identify the operational limits of the ‘clean’ supersonic combustion mode, steady numerical simulations were carried out using various pressures in the hydrogen injector plenum. The plenum pressure was increased from 3 bar to 8 bar in steps of 1 bar, resulting in equivalence ratios from 0.14 to 0.47.

In figure 5(a) we show pressure distributions on the injector-side combustor wall for the different equivalence ratios. The general trend is for the overall pressure rise to increase for higher equivalence ratios, as the additional fuel leads to a greater heat release. No converged CFD solution could be obtained for the largest equivalence ratio (the dashed pressure distribution in figure 5(a)), since in this case a separated flow region developed on the injector-side wall and subsequently moved upstream, causing strong oscillations in the flow field and preventing the CFD solution from converging to a steady state.

As outlined in § 1, the two general operational limits that can lead to choking of the combustor flow and potentially to unstart of scramjet engines are thermal choking and boundary-layer separation. An integral thermal choking limit was estimated for the present combustor-entrance conditions using a control-volume analysis and assuming ideal equilibrium combustion. Approximations for the skin friction and heat loss through the cold combustor walls, calculated from the CFD solutions, were included. According to this analysis, thermal choking occurs at an equivalence ratio of 0.49, corresponding to a combustor pressure rise of $p/p_i = 3.81$, where p_i is the pressure at the inlet. This estimate does not include the pressure rise from the hydrogen injection and assumes the heat addition to take place uniformly over the duct cross-section. Note that only the choking equivalence ratio, and not the corresponding pressure rise, relies on the assumption of complete combustion.

Limits for the shock-induced separation of turbulent boundary layers have been proposed by several researchers, for example, Love (1955) and Korkegi (1975). Frost *et al.* (2009) suggested that the Korkegi criterion can also be applied to the more gradual pressure rises experienced in scramjet combustors. According to this criterion, the critical pressure ratio at which flow separation occurs is given by

$$p/p_i = \begin{cases} 1 + 0.3M_i^2 & \text{for } M_i \leq 4.5, \\ 0.17M_i^{2.5} & \text{for } M_i > 4.5, \end{cases} \quad (4.1)$$

where M_i is the inlet Mach number. For the present configuration, this gives a critical pressure ratio of 2.9. Heiser & Pratt (1994) cite the Love criterion, $M/M_i < 0.762$, for illustration, without recommending its use for design purposes; for the HyShot II combustor entrance conditions, it predicts an earlier onset of separation than the Korkegi criterion. In either case, we are led to the same conclusion as Frost *et al.* (2009): that choking of the HyShot II combustor should be initiated by boundary-layer separation rather than thermal choking. This conclusion is also consistent with the qualitative combustion behaviour in the steady computations just discussed.

An analysis of the steady computational results was performed in order to determine where the combustor flow conditions lay relative to these limits at the various equivalence ratios. The pressure rise was calculated in each case using a stream-thrust averaging approach. In addition, a theoretical equilibrium pressure rise was determined using a control-volume analysis, assuming complete combustion and including estimates of frictional and heat-loss effects from the computations (as just described for the calculation of the thermal choking limit). These results are plotted in figure 5(b) together with the thermal choking and Korkegi limits; also shown are the peak pressures on the injector and cowl-side walls. It is immediately apparent that the equilibrium analysis significantly overestimates the average pressure rise in the combustion chamber for all but the lowest equivalence ratio. This is because, contrary to the assumption of complete combustion independent of the equivalence ratio, the combustion efficiency decreases markedly with increasing ϕ : the amount of unburned hydrogen at the combustor exit increases from 7.8% for $\phi = 0.14$ to 26% for $\phi = 0.41$. Thus, whereas the control-volume analysis predicts the onset of thermal choking at $\phi = 0.49$, the stream-thrust-averaged profile is well below the critical pressure ratio at which this would occur. Moreover, the latter profile is still below the Korkegi limit at the highest ϕ considered, although the local maximum pressures on both the injector and cowl-side walls have exceeded this value. In fact, the Korkegi limit applied to the injector-side wall appears to give a good indication of the onset of separation in the steady-state computations. That separation occurs first on the injector-side wall rather than on the cowl-side wall, despite the higher maximum pressure on the latter, is probably because the peak pressure on the cowl-side wall occurs at the first impingement location of the injector barrel shock and is followed by an expansion that rapidly decreases the pressure and re-stabilizes the boundary layer. On the injector-side wall, the boundary layer has already been disturbed by the injected hydrogen and thus is more prone to separation.

5. Unsteady combustion

5.1. Experimental results

In previous experimental studies involving the HyShot II configuration (Hannemann *et al.* 2008; Frost *et al.* 2009), unsteady choking of the combustor was found to

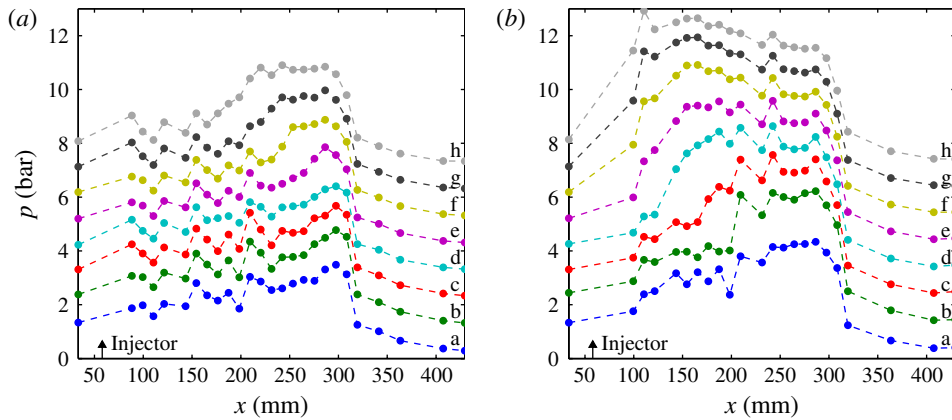


FIGURE 6. (Colour online) Unsteady experimental pressure development inside the combustion chamber for equivalence ratios of (a) 0.50 and (b) 0.64. The measurements are made on the injector-side wall and are at times (a) 2.4, (b) 2.6, (c) 3.0, (d) 3.4, (e) 3.8, (f) 5.2, (g) 5.6 and (h) 6.6 ms in both plots. For clarity, all traces except the first in each plot have been shifted upwards by an integral number of bars.

occur as the equivalence ratio was increased above a value of approximately 0.5. The onset of choking took the form of a pressure disturbance that developed in the rear of the combustor and began to propagate upstream. Based on a simple Rayleigh-flow analysis, Frost *et al.* (2009) ruled out thermal choking as a possible source of this unsteady behaviour and assumed boundary-layer separation to be responsible.

Similar behaviour was noted in the present experiments. In figure 6, we show examples for equivalence ratios of 0.50 and 0.64: in each case, the pressure distribution on the injector-side wall is plotted at various times in the relevant experiment. For $\phi = 0.5$, a gradual pressure rise initially extends down the duct ($t = 2.4$ ms), reaching a level slightly exceeding the maximum pressure for $\phi = 0.33$. This pressure rise subsequently steepens towards the rear of the combustor and, from around $t = 3.8$ ms, begins to propagate upstream. By the last time shown ($t = 6.6$ ms), the onset of the pressure rise has reached approximately the midpoint of the duct, $x \approx 170$ mm. For $\phi = 0.64$, the unsteady behaviour is similar but occurs on a much-compressed time scale and involves higher pressures. The initial profile shows a somewhat steeper rise than for the lower equivalence ratio, plateauing close to $x = 250$ mm at a level almost three times the entrance pressure. This pressure rise steepens further and begins to propagate up the duct almost immediately. By the end of the test time (~ 6 ms), a sharp pressure jump has developed immediately downstream of the injection location, followed by an extended plateau region. At $t = 6.6$ ms, however, the pressure rise has still not reached the transducer upstream of the injection port-holes.

5.1.1.1. The case $\phi = 0.6-0.7$

We concentrate first on experimental results for $\phi = 0.6-0.7$, as the largest amount of data was gathered in this range of equivalence ratios. In order to further elucidate the behaviour of the transient system responsible for the time-developing pressure profiles in figure 6, in figure 7 we plot time-resolved pressure traces at various positions on the cowl-side wall for the same experiment. Following the initial pressure rise signalling the arrival of the test flow, strongly oscillatory signals are visible

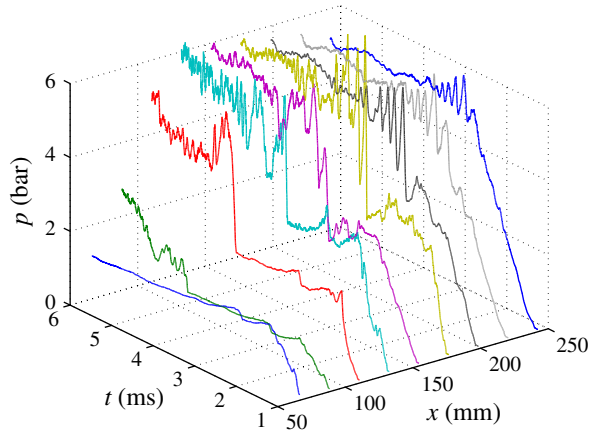


FIGURE 7. (Colour online) Time-resolved pressure traces at various positions on the cowl-side combustor wall for an equivalence ratio of 0.64.

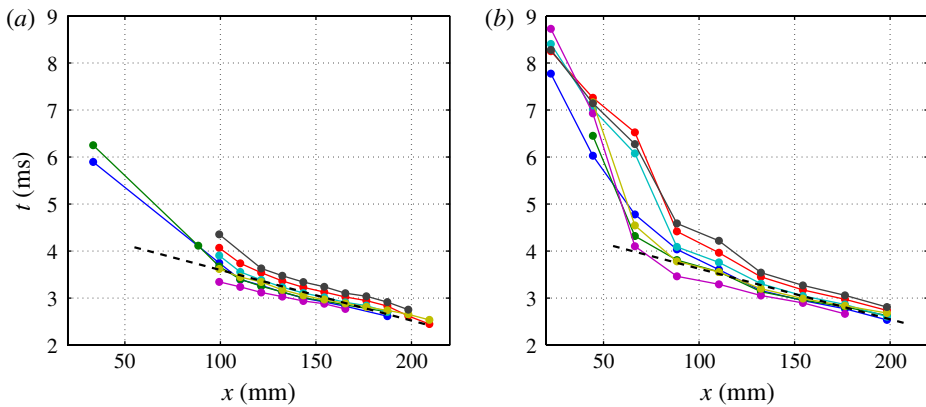


FIGURE 8. (Colour online) $X-t$ diagrams showing the motion of the leading edge of the unsteady shock train in the combustor for shots with equivalence ratios of $\phi \approx 0.66$: (a) injector-side wall; (b) cowl-side wall. The dashed line in each case indicates a propagation speed of 93 m s^{-1} .

at the downstream pressure stations, with the amplitude of the oscillations reaching a maximum near $x = 176 \text{ mm}$. This suggests the development of moving periodic flow structures, in particular, the propagation of an unsteady shock train up the combustor. Upstream of $x = 176 \text{ mm}$, the periodic structures become progressively less well defined and eventually form just a single sharp rise followed by residual unsteadiness, indicating a breakdown in the shock-train structure.

In figure 8 are plotted $x-t$ diagrams showing the motion of the leading edge of the shock system on both the injector and cowl-side walls, as determined by the arrival of the corresponding pressure rise at each transducer. Results from seven experiments with calculated equivalence ratios of 0.66 ± 0.04 are shown. In all cases, the upstream motion begins before the nominal start of the steady test time (3.5 ms), but, as noted earlier, the test flow may be considered to be approximately steady by 2.5 ms. The

speed of propagation is approximately constant between $x \approx 200$ and 120 mm, with a slight upward concavity indicating that the system is gradually slowing as it moves forwards. From $x \approx 120$ mm, this slowing becomes more pronounced and is typically followed by a pause in the upstream motion somewhere between 44 and 84 mm (this is seen most clearly in the cowl-side traces). Following the conclusion of the test time (6 ms), the shock system continues to move upstream of the injector at a speed significantly below that with which it propagated downstream of injection. We note here that the injection pressure remains approximately constant for some 25 ms after the end of the test time, whereas the reservoir pressure decreases monotonically during this period (see figure 1), thus leading to a continual increase in the effective equivalence ratio. In both plots of figure 8, a line is shown with a slope corresponding to a propagation speed of 93 m s^{-1} ; this matches well with the speed of the system in the initial part of its upstream motion.

We now turn to the high-speed schlieren and OH^* visualizations recorded during this period of unsteady development. Correlating the flow and combustion features visualized using these two techniques was complicated by the fact that, as mentioned in § 2.3, only one or the other could be applied in a given experiment. Nevertheless, by comparing the shock-train motions plotted in figure 8, the effective time offset between pairs of experiments could be determined. It should be kept in mind in interpreting these images that both techniques are line-of-sight and that the flow field is highly three-dimensional.

In figure 9, we show sequences of schlieren and OH^* visualizations of the flow region immediately downstream of the injector ($x = 56\text{--}136$ mm). The picture is initially similar to that for $\phi = 0.33$, except with a higher degree of injectant penetration and stronger injection-related shocks caused by the increased mass flow of hydrogen. Weak combustion is again visible in the OH^* image in areas close to the injector-side wall, where reflections of the injection barrel shock impinge on the hydrogen jet (note that the exposure time here is significantly shorter than in figure 4). By $t = 3.5$ ms, the arrival of the upstream-propagating shock system is visible in the schlieren image. Corresponding to this, a bulging structure appears in the OH^* visualization, slightly preceding the shock visible on the cowl-side wall. This structure suggests the development of boundary-layer separation on the injector-side wall, since the increased residence time in a separated flow region will enhance ignition and lead to increased levels of OH^* production.

The shock train continues to propagate upstream until approximately 4.4 ms, whereafter the combustor flow appears to find a quasi-stable configuration with an oblique shock lodged on the cowl-side wall approximately three duct heights downstream of the injector. A region of intense combustion then begins immediately downstream of the impingement location of this shock on the injector-side wall. Unsteady flow structures, suggesting the presence of large-scale flow separation in this region, are observed in the schlieren images. Because of the limited test time, it is difficult to conclude whether this configuration is truly stable or simply a transient quasi-stable flow topology. Following the conclusion of the test time (6.0 ms), the shock system continues moving upstream past the injection point. It is not clear, however, whether this is caused entirely by the increasing effective equivalence ratio or if, given sufficient time at a constant equivalence ratio, such behaviour would develop regardless. Comparing the schlieren and OH^* images at 4.4 and 5.6 ms, it is apparent that, although the position of the cowl-side shock is relatively fixed, the combustion downstream is intensifying, which in itself could eventually lead to further upstream propagation of the shock train. Such quasi-stable shock-propagation behaviour has

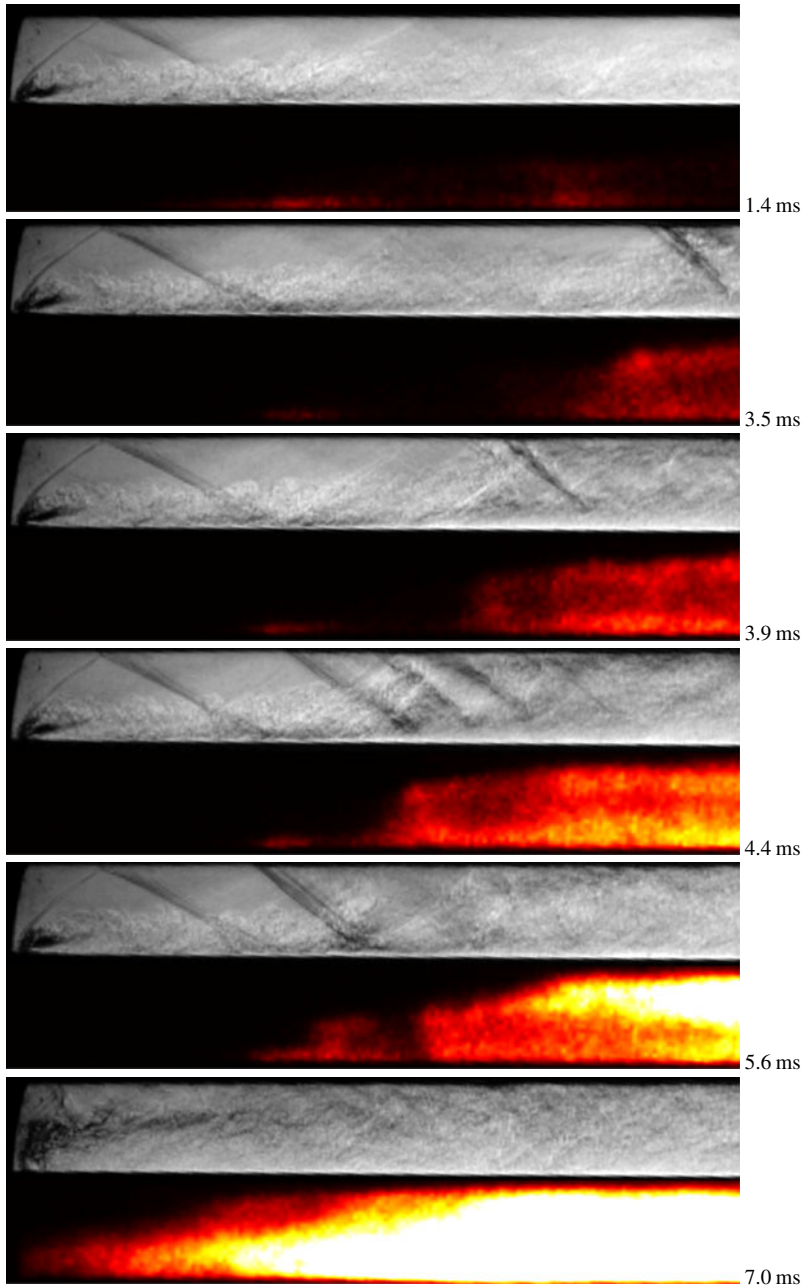


FIGURE 9. Sequences of quasi-synchronous schlieren and OH* chemiluminescence images of the flow near the injector ($x = 56\text{--}136$ mm) for an equivalence ratio of $\phi \approx 0.66$.

been noted previously, for example, by Do *et al.* (2011) during duct experiments in which choking was induced by mass addition.

Having examined the transient shock system as it approaches the injection location, we now look to the origin of this system in the central combustion chamber in the sequence of figure 10. For this particular OH* sequence, the camera was focused

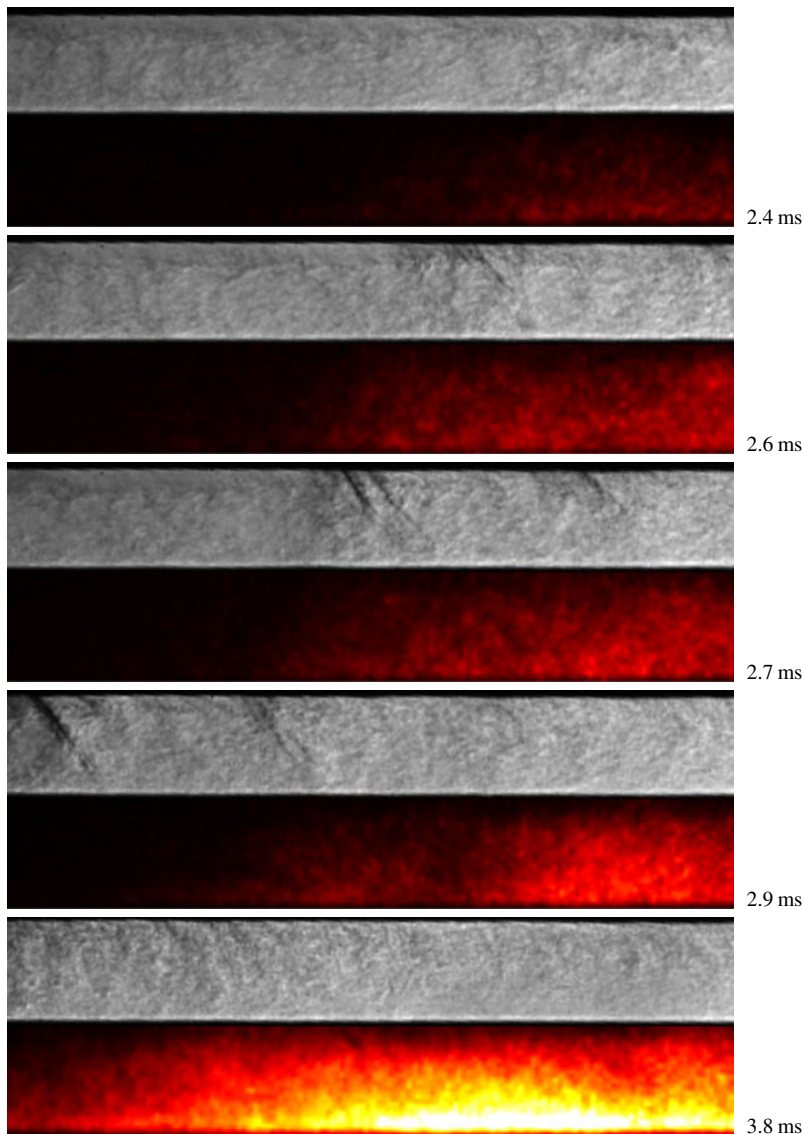


FIGURE 10. Sequences of quasi-synchronous schlieren and OH* chemiluminescence images of the flow in the central combustion chamber ($x = 158\text{--}228$ mm) for $\phi \approx 0.66$.

on the combustor sidewall rather than the midplane, which tended to accentuate combustion features close to the injector-side wall. As suggested by the pressure traces in figure 7, the nascent system takes the form of an unsteady shock train that propagates up the duct ($t = 2.6\text{--}2.9$ ms). The individual structures in this shock train are most visible on the cowl-side wall – probably because the lateral extent of the supersonic flow region is greatest in this part of the combustor – but it is apparent in several of the schlieren images that parts of the shock system extend over the height of the duct. The appearance of the system is quite different from that of the canonical bifurcated shock train associated with shock–boundary-layer interactions in

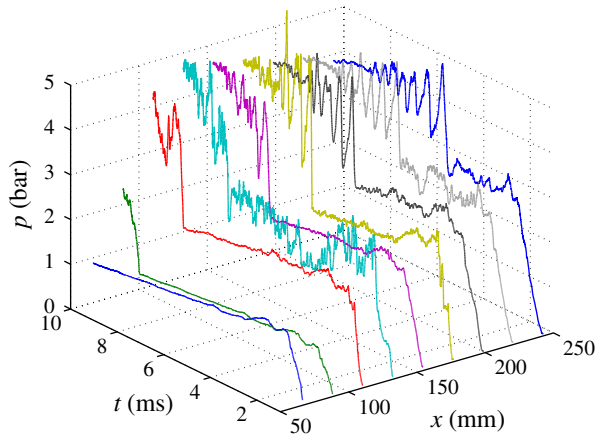


FIGURE 11. (Colour online) Time-resolved pressure traces at various positions on the cowl-side combustor wall for an equivalence ratio of 0.5.

internal geometries (Matsuo, Miyazato & Kim 1999), and this is no doubt partly due to the highly three-dimensional nature of the flow. Nevertheless, the trailing cowl-side shocks in the train do not appear to be significantly displaced from the wall, which would be expected if boundary-layer separation were playing a crucial role here. Moreover, in comparing the schlieren and OH^* images, we note that, although the onset of the shock system appears to be related to the intensification of combustion within the duct, there are no strong combustion features on the injector-side wall that follow the movement of the shock train upstream. In particular, if large-scale separation of the boundary layer were driving the shock system up the combustor, we would expect the separated regions to be visible as strong features moving upstream in the OH^* images, as already seen in the sequence of figure 9. No such features are observed here, suggesting that boundary-layer separation, if at all present, is limited to localized bubbles, which are unlikely to be capable in themselves of producing the observed behaviour. We thus conclude that the primary mechanism responsible for the development of the transient shock system is thermal choking, rather than boundary-layer separation. Following the propagation of the shock train out of the visualization window, steadily increasing levels of OH^* are observed, indicating that the combustion is continuing to intensify. The apparent absence of boundary-layer separation in this sequence suggests that the onset of the separated region presumed to be present in the upstream sequence probably occurred in the area between the two visualization windows, i.e. between 136 and 158 mm. The breakdown in the shock-train structure observed in figure 7 may be linked to the development of this separated region.

5.1.2. The case $\phi = 0.5$

Two experiments were performed with equivalence ratios of approximately 0.5. In figure 11 we show time-resolved pressure traces on the cowl-side wall from one of these. The development of the oscillatory pressure signals towards the rear of the combustion chamber is similar to that of the $\phi = 0.66$ case shown in figure 7, again indicating the formation of an upstream-propagating shock train. Now, however, the periodic structures are already well developed at the most downstream point shown ($x = 242$ mm), indicating that the shock train has originated from further down the combustor. The speed of propagation during the steady test time is also slower: a value

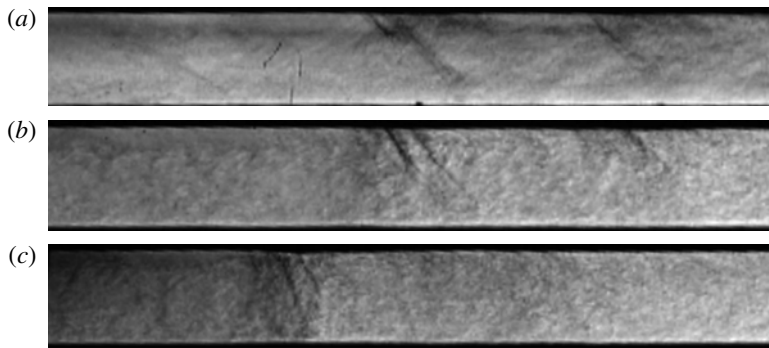


FIGURE 12. Schlieren images showing shock trains developing in the central combustion chamber: (a) $x = 123\text{--}205$ mm at $t = 7.3$ ms for $\phi = 0.50$; (b) $x = 158\text{--}228$ mm at $t = 2.7$ ms for $\phi = 0.66$; (c) $x = 137\text{--}212$ mm at $t = 2.1$ ms for $\phi = 1.1$.

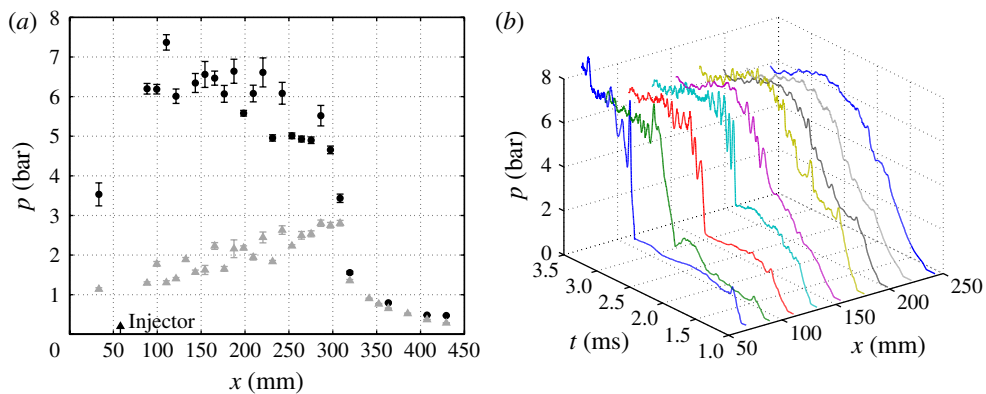


FIGURE 13. (Colour online) (a) Mean pressure profiles on the injector-side combustor wall for equivalence ratios of 1.0 (●) and 0.33 (▲), averaged over the steady test time. (b) Time-resolved pressure traces at various positions on the cowl-side wall for $\phi = 1.1$.

of approximately 31 m s^{-1} was estimated from $x\text{--}t$ diagrams. Schlieren visualizations were captured of the propagation of this shock train in the central combustion chamber, and in figure 12 one of these is compared with corresponding images for $\phi = 0.66$ and 1.1. The appearance of the shock structures is similar for the lower two equivalence ratios, which, together with the qualitatively similar time-resolved pressure traces, suggests the same mechanism to be responsible. No OH^* images were recorded for $\phi = 0.5$.

5.1.3. The case $\phi = 1.0\text{--}1.1$

Experiments were also carried out at higher equivalence ratios in the range of 1.0–1.1, the intention being to have the combustor fully choked during the steady test time. In figure 13(a) is shown the static pressure distribution (averaged over the test time) on the injector-side wall from an experiment with $\phi = 1.0$. This is compared with the $\phi = 0.33$ measurements already seen in figure 3. Instead of the gradually increasing pressure levels indicative of supersonic combustion, much higher pressure

levels are now observed throughout the combustion chamber (extending upstream of the injection point), with a generally decreasing trend downstream of injection. This is consistent with subsonic combustion inside the combustor. The sharp drop in pressure observed in the expansion region ($x > 300$ mm) indicates that a sonic throat is formed at the exit of the constant-area section, with supersonic flow further downstream.

Although, for these highest equivalence ratios, the upstream propagation of the unstart shock train was complete before the beginning of the steady test time, it is still instructive to compare the propagation characteristics with the other equivalence ratios studied thus far. In figure 13(b) we show unsteady pressure traces on the cowl-side wall for an experiment with $\phi = 1.1$. The development is similar in some senses to the pictures in figures 7 and 11, but on a much-compressed time scale. Again, oscillatory profiles are observed in the pressure traces, but these begin further upstream ($x \approx 150$ mm) than in either of the previous cases, indicating that the shock train is forming further up the combustor. Downstream of this, pressure rises without significant oscillations are observed. The propagation speed of the shock train was approximately 220 m s^{-1} in these experiments.

In figure 14 is shown a sequence of quasi-synchronous schlieren and OH* visualizations of the flow immediately downstream of the injector. The combustion region accompanying the propagating shock system now appears both more intense and more strongly coupled to the leading shock in the train than for $\phi = 0.66$. As the system moves upstream, it appears to hesitate near the quasi-stable position of the $\phi = 0.66$ development ($t = 2.6$ ms), but then quickly moves further upstream past the injector, suggesting that the heat release is too intense for this flow topology to persist. By 3.2 ms, the entire visible portion of the duct is choked, with a region of intense combustion directly downstream of the injector. The lack of visible shocks in the schlieren image suggests that the flow is now subsonic, consistent with the decreasing pressure trend in figure 13(a).

For these high-equivalence-ratio experiments, the most upstream pressure transducer, located 22 mm downstream of the leading edge of the injector-side wall, registered the passage of the shock train slightly before the beginning of the steady test time. However, a thermocouple located on the cowl-side wall directly opposite the injector-side leading edge did not show the passage of the shock train until after the conclusion of the test time, just prior to the onset of the unsteady oscillations discussed in § 6. These observations suggest that, during the test time, the shock system was lodged at the entrance to the combustion chamber, without fully unstarting the inlet. As the junction between the intake ramp and the combustor entrance was open both to the sides and through the boundary-layer bleed channel, a shock sitting at this position would allow the combustor entrance conditions to be modified without affecting the intake flow. Such a flow configuration was visualized in preliminary unfuelled experiments in which insufficient drainage of the boundary-layer bleed channel had been provided, but unfortunately, in the fuelled experiments, no visualizations of the combustor entrance were available to support this interpretation.

In figure 12, a schlieren image showing the incipient shock train in the central combustion chamber for a $\phi = 1.1$ experiment is compared to images from the lower equivalence ratios already discussed. Although the appearance of the shock train is again generally similar, the leading shock in the train is now noticeably steeper; also, the trailing shocks are less visible, which is consistent with the decreased strength of the oscillations seen in figure 13(b) as compared with figures 7 and 11. This may be indicative of the closer coupling between ignition and shock structure suggested by figure 14, as rapid heat release immediately behind the leading shock will drive

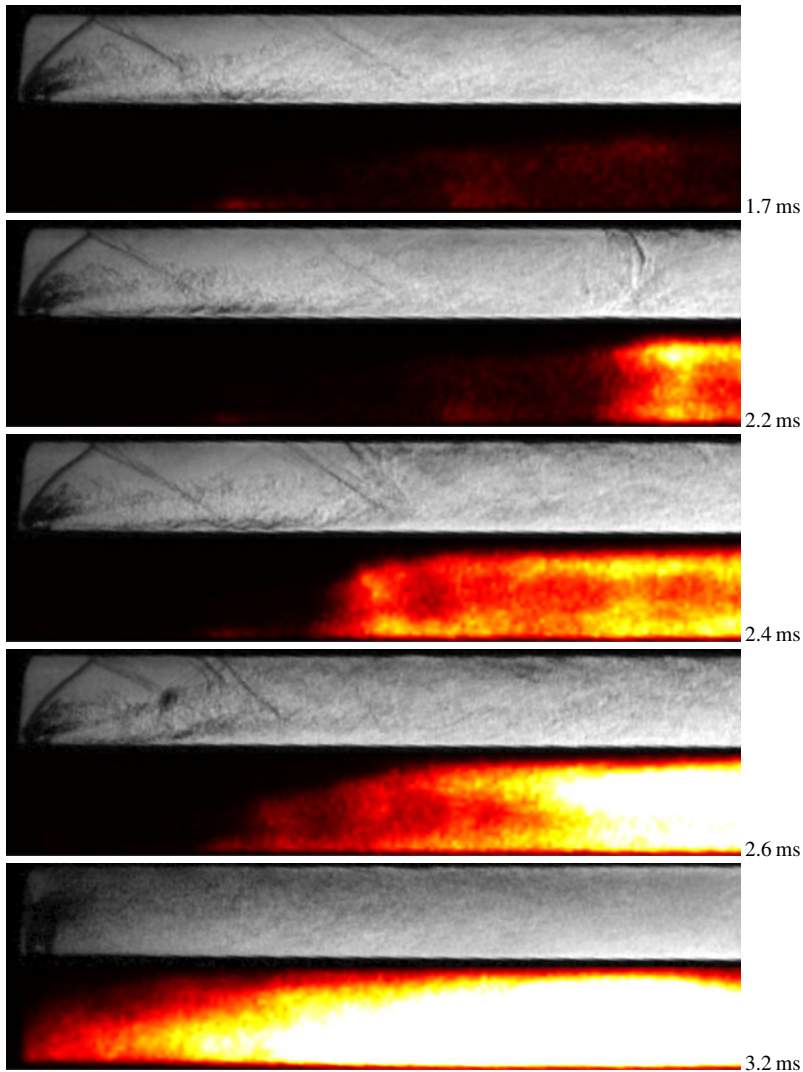


FIGURE 14. Sequence of quasi-synchronous schlieren and OH* chemiluminescence images of the flow near the injector ($x = 56\text{--}136$ mm) for an equivalence ratio of 1.1.

the Mach number towards unity and decrease the strength of any secondary shocks. The fact that such trailing shocks are still present, however, indicates that the flow downstream of the leading shock is still supersonic and that conditions for a self-sustaining detonation wave have not yet been reached.

5.2. Numerical simulations

In order to gain further insight into the transient unstart phenomena just described, and, in particular, to help isolate the mechanism responsible, unsteady CFD simulations were performed. The following simplified model problem was chosen, both to minimize the computational cost and because of uncertainty in the exact flow conditions during the experimental start-up process. A steady-state initial solution was

first obtained for the largest stable equivalence ratio determined in § 4.2 ($\phi = 0.412$). The inflow pressure was then reduced as

$$p(t) = \begin{cases} p_f - (p_f - p_0)(1 - t/t_i)^2 & \text{for } t \leq t_i, \\ p_f & \text{for } t > t_i, \end{cases} \quad (5.1)$$

and similarly for the inflow density $\rho(t)$, with the inflow temperature, the inflow velocity and the injection pressure remaining unchanged. Here, p_f was specified so as to match the computed experimental inflow pressure; the injection pressure was chosen to give the desired final equivalence ratio (after time t_i). The use of (5.1) provided a smooth transition between the initial and final equivalence ratios, and, with a chosen t_i of 1 ms, was intended to roughly simulate the reduction in test-section pressure during the HEG start-up process seen in figure 1. A dual time-stepping scheme with second-order temporal accuracy and a physical time step of 0.1 μs was applied.

In figure 15, we show numerical results highlighting the flow features within the combustor at four time instants during the unsteady development for a final equivalence ratio of 0.715, intended to approximately match the $\phi = 0.66$ experiments. The total injection pressure for this simulation was 12.0 bar. At each instant, the colour visualization shows contours of OH mass fraction, with streamlines emanating from the injector indicated in black. On the lateral cut planes, sonic lines are shown in red; boundaries of negative streamwise velocity indicating regions of separated flow are shown as red surfaces. Pseudo-schlieren (i.e. density-gradient magnitude) images on three equally spaced planes are also shown, the first and third planes being the lateral boundaries of the computational domain. On these images are superimposed sonic lines (blue) and boundaries of flow reversal (red). Pressure distributions on the injector-side wall corresponding to these visualizations are shown in figure 16(a).

At $t = 0.01$, the expected shock pattern extends down the duct. A significant subsonic region develops over a narrow zone downstream of the injection port-hole, but subsonic flow is limited to the wall boundary layers throughout the remaining combustor domain. In the OH image, we see that the sonic line on each lateral cut plane lies below the main combustion region centred at the shear layer between the incoming air and the injected hydrogen. Thus, combustion is taking place under principally supersonic conditions at this time. No flow separation is visible.

At the second instant shown ($t = 0.8$ ms), the subsonic region on the injector plane has grown considerably to encompass the entire combustor height and has also expanded laterally. The shock system near $x = 150$ cm has strengthened significantly and already begun to propagate upstream; a steep rise is also visible in the corresponding pressure trace in figure 16(a). A small localized separation bubble has just begun to develop on the injector-side wall, visible midway down the combustor on the injector plane, but this is clearly not responsible for the formation of the propagating shock train. The OH visualization shows that flow conditions in the main combustion region are now almost completely subsonic by the fourth cut plane downstream, or, more correctly, that the heat release in this region has driven the flow to subsonic conditions by this point downstream. In other words, the conditions for thermal choking have been attained locally in the stream tube containing the main combustion region. At $t = 1.0$ ms, additional separation bubbles are visible both on the cowl-side wall and further downstream on the injector-side wall. Of further note is the embedded region of flow reversal in the middle of the combustor: this feature would explain the ‘two-tiered’ appearance of the experimental OH* structures as the shock system approaches the injector in figure 9 ($t = 3.5$ and 3.9 ms).

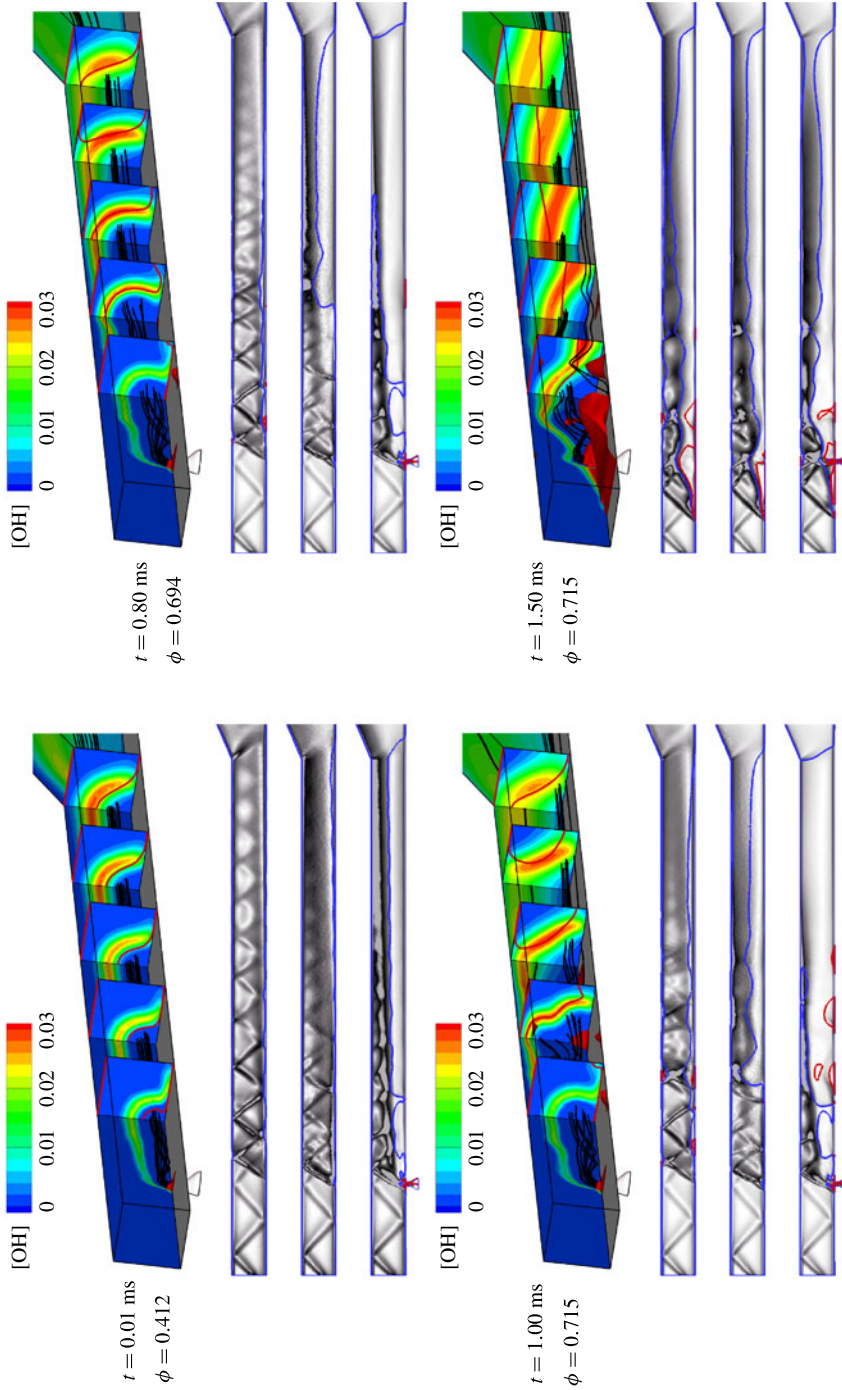


FIGURE 15. Numerical results of the HyShot II combustor choking process at different time instants for a final equivalence ratio of 0.715. In colour are shown contours of OH mass fraction, together with sonic lines (red), streamlines emanating from the injector (black) and boundaries of flow reversal (red surfaces). Also shown are pseudo-schlieren images on three equally spaced cut planes, with sonic lines (blue) and flow reversal boundaries (red) also indicated. The axial coordinate in all images has been compressed by a factor of two.

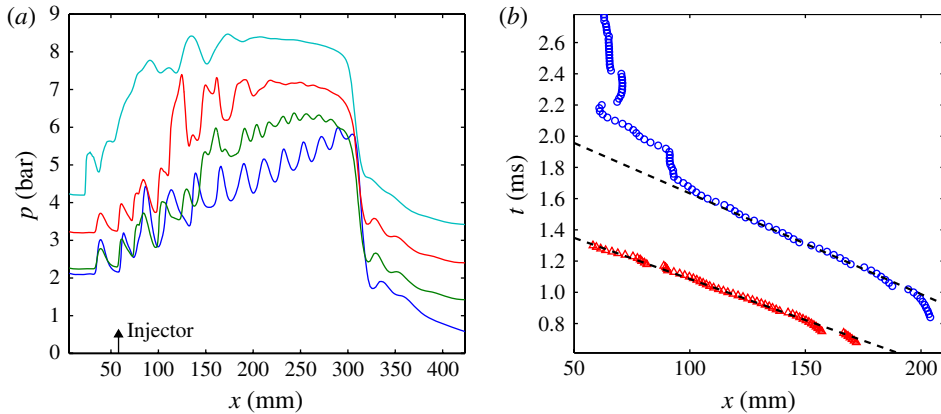


FIGURE 16. (Colour online) (a) Pressure distributions on the symmetry line of the body-side combustor wall for the $\phi = 0.7$ numerical simulation at the time instants shown in figure 15 (lowermost, $t = 0.01$ ms; uppermost, $t = 1.5$ ms). All but the the first profile have been shifted upwards by an integral number of bars. (b) Motion of the leading shock in the unsteady shock train on the cowl-side wall for equivalence ratios of $\phi = 0.553$ (\circ) and 0.715 (\triangle); the dashed lines indicate propagation speeds of 155 and 190 m s^{-1} .

In contrast to the corresponding experiments, no significant pausing of the shock-train motion is observed near the injection location. The shock motion continues upstream of the injectors ($t = 1.5$ ms), but now as a two-dimensional shock train associated with large-scale flow separation on the injector-side wall. An embedded supersonic region remains, extending down the entire length of the combustor. The corresponding pressure profile in figure 16(a) shows a pressure rise beginning upstream of the injector, followed by an extended plateau. The instantaneous flow configuration here is similar to a dual-mode scramjet with an oblique shock train located in the isolator.

In figure 16(b), we plot the motions of the leading shocks on the cowl-side wall from both this and another simulation to be discussed shortly. The shock positions were estimated by setting an appropriate pressure threshold and, at each time step, calculating the first downstream point at which this threshold was exceeded. The formation point of the incipient shock train (~ 170 mm) is somewhat upstream of the corresponding point in experiments (~ 200 mm). The numerical shock accelerates as it forms but soon reaches a roughly constant speed; the plotted line shows this to be approximately 190 m s^{-1} , significantly higher than in the experiments. A similar discrepancy with experimental results was obtained by Sunami & Kodera (2012). Small hesitations are observed as the shock train approaches the injector ($x = 80$ – 90 mm), but the obvious slowing seen in figure 8 is not present. As a result of both the absence of pausing and the higher overall propagation speed, the shock train has reached the injection location within ~ 0.6 ms of its formation, much more quickly than in experiments. Possible explanations for these discrepancies are discussed in § 8.

To examine the effects of varying the equivalence ratio on the unsteady behaviour in the numerical model, a further simulation with a final value of $\phi = 0.553$ was performed (total injection pressure, 9.30 bar). The transient development again appeared to be triggered by the sonic line crossing the main combustion region towards the rear of the combustor. In this case, the formation of the unsteady

shock train was accompanied immediately by a separation bubble on the injector-side wall, which followed the shock train upstream. The extent of the separated regions again remained limited, however, and, while they may have promoted the choking development by providing an effective area contraction, it was once more evident that boundary-layer separation was not the primary driving mechanism. In contrast to the higher-equivalence-ratio simulation, once the leading shock reached and merged with the injector barrel shock, the flow thereafter attained a quasi-stable configuration with no further propagation of the shock train. This behaviour is similar to that observed in the $\phi = 0.66$ experiments, though the resulting flow topologies differ.

The motion of the leading shock on the cowl-side wall is plotted in figure 16(b). Compared to the higher equivalence ratio, the shock train now originates further back in the combustor (from ≈ 200 mm) and propagates upstream at a slower speed: the dashed line indicates a value of 155 m s^{-1} . A deceleration of the shock system is seen from approximately 120 mm, similar to the experimental behaviour for $\phi = 0.66$. (In the $\phi = 0.5$ experiments, the test period had already concluded by the time the shock train had reached a comparable point upstream, so no comparison can be made here.) This deceleration is followed by the termination of the upstream motion when the shock system merges with the injection shock. A large discrepancy is again obtained between the experimental and numerical shock-propagation speeds.

6. Inlet unstart

As stated in § 5.1.1, the effective equivalence ratio increases monotonically after the conclusion of the test time owing to the falling reservoir pressure. For clarity, in this section we thus refer to the steady equivalence ratio (i.e. the average value during the test time, which has simply been denoted ϕ thus far) as ϕ_s , with ϕ_u referring to the time-varying quantity. At some point after the test time in all combustion experiments, large-scale pressure oscillations were observed to develop inside the combustion chamber. The exact time at which these oscillations first appeared depended on the steady equivalence ratio: for $\phi_s = 1.1$ experiments, the onset occurred as early as 2 ms after the end of the steady test period, whereas for lower steady equivalence ratios it was somewhat later. Figure 17(a) shows one example of the observed oscillatory behaviour: here, the unsteady equivalence ratio is plotted together with time-resolved pressure traces at several positions on the injector-side wall for a $\phi_s = 1.1$ experiment. The oscillations from roughly 8 ms are similar to those documented, for example, by Tan & Guo (2007) and Wagner *et al.* (2009) for an unstarted inlet. This oscillatory behaviour is often referred to as ‘buzzing’ and is caused by periodic gorging and disgorging of the inlet shock system. At the onset of the oscillations, the unsteady equivalence ratio has risen to approximately 1.2; for $\phi_s = 1.1$, onset values between 1.2 and 1.3 were found to be typical. In $\phi_s = 0.66$ experiments, the first appearance of buzzing was later, typically between 11 and 12 ms, and at lower unsteady equivalence ratios of between 0.9 and 1.0. In figure 17(a), the oscillations are clearly visible in the traces of the three transducers downstream of the injection location. Although they are less clear in the trace from upstream of the injection point, the power spectrum of this signal showed peaks similar to those in the downstream traces. Also apparent in the oscillatory profiles is a phase-shift between measurement locations due to the lag from the pressure signal travelling down the duct.

Before proceeding further, a brief discussion of the use here of data beyond the steady test time is warranted. In general, post-test-time data from shock tunnels should be treated with caution, particularly if driver-gas contamination has altered the free

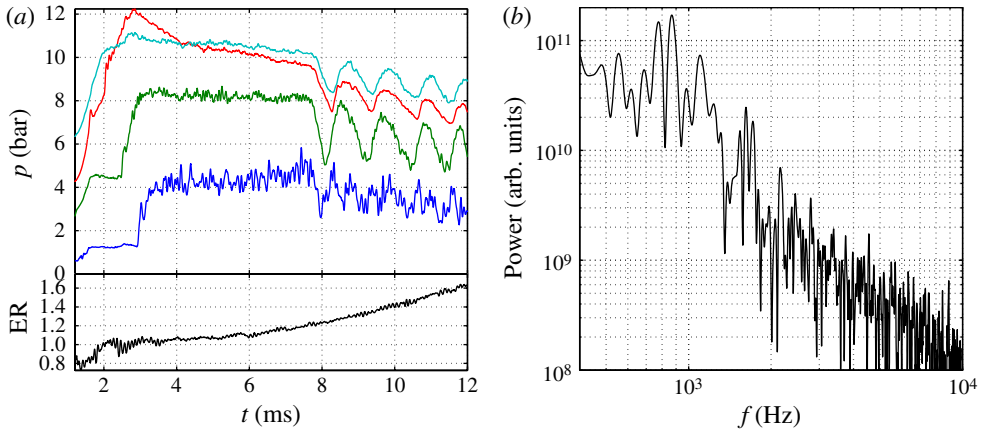


FIGURE 17. (Colour online) (a) Time-resolved pressure development inside the combustor compared to the temporal development of the equivalence ratio. The pressure traces are on the injector-side wall at x locations of 33 (lowermost), 88, 187 and 297 mm (uppermost); all but the first trace have been vertically shifted for clarity. (b) Power spectrum of the pressure trace at 88 mm during the ‘buzzing’ phase.

stream composition. In § 2.1, we concluded that the flow has not been significantly contaminated by driver gas until at least 12 ms. Both the pressure and temperature, however, are falling monotonically from around 6 ms due to the arrival of expansion waves in the reservoir. For combusting applications, changes in temperature may be of particular concern, since reaction rates can vary exponentially with temperature. Nevertheless, as the expansion in the reservoir is isentropic, changes in temperature will be more gradual than those in pressure: for example, a 20% drop in pressure will correspond to just a $\sim 5\%$ decrease in temperature. Moreover, as the combustor-entrance temperature here is relatively high (1300 K), ignition characteristics will be determined largely by mixing constraints rather than chemistry. We also note, relevant to the present section, that the buzzing phenomenon is primarily aerodynamic and aeroacoustic in nature, rather than fundamentally combustion-related (as evidenced by its having been observed in non-combusting facilities). Thus, the precise combustion characteristics during the buzzing phase are of limited importance for the present discussion.

In figure 17(b) is shown a typical power spectrum, taken from the transducer located at 88 mm. We observe a group of peaks close to 1 kHz, with the strongest centred at 870 Hz; weaker harmonics can be discerned near 1.7 kHz. Assuming the oscillations to be acoustic in nature, we may estimate the resonant modes, following Newsome (1984), by considering waves (compression or expansion) travelling at speeds $\bar{a} + \bar{u}$ and $\bar{a} - \bar{u}$, respectively, up and down the combustor. Here \bar{a} is the mean sound speed and \bar{u} is the mean flow velocity, each averaged in an appropriate manner. The frequencies of the fundamental and higher modes for a duct of length L that is open at both ends are then

$$f_n = \frac{n\bar{a}}{2L}(1 - \bar{M})(1 + \bar{M}), \quad n = 1, 2, 3, \dots, \quad (6.1)$$

where $\bar{M} = \bar{u}/\bar{a}$. For the present model, the length of the duct (from the cowl leading edge to the end of the constant-area section) is 367 mm. The speed of the

pressure disturbance propagating in the downstream direction, $\bar{a} + \bar{u} = \bar{a}(1 + \bar{M})$, can be estimated by correlating the oscillatory pressure signals between different measurement locations. The speed thus determined was found to increase down the duct, as would be expected for heat addition in a constant-area subsonic flow, with a mean value of approximately 1600 m s^{-1} between 88 and 297 mm. This probably overestimates the overall mean speed (including the section ahead of the injector), so we assume a representative value of 1500 m s^{-1} . It thus remains to estimate $1 - \bar{M}$, which we do as follows. We have already noted that the core flow (i.e. outside the wall boundary layers) is sonic at the exit of the constant-area section. The conditions at the combustor entrance depend on the intake shock structures, which are here imposed by the downstream subsonic flow, but the entrance Mach number is relatively insensitive to the exact nature of these shock structures. For example, a single strong shock at the inlet (with a deflection angle of 3.6°) gives a post-shock Mach number of 0.40, whereas a weak shock with a turning angle of 21.6° (i.e. the ramp angle) followed by a strong shock gives a value of 0.49. Since unstart is characterized by a displacement of the original shock system out of the inlet, the former value is probably more appropriate. Thus, assuming $M = 0.4$ until the injector, rising to $M = 1$ at the exit, a mean value of $\bar{M} = 0.6$ seems reasonable and is probably accurate to within 0.1. Substituting these estimated values into (6.1) gives $f_1 = 820 \text{ Hz}$, which, considering the approximations made in the analysis, agrees well with the observed band of frequencies.

7. Discussion of experimental and computational results

As noted in § 5.1, Frost *et al.* (2009) interpreted the unsteady choking phenomena in the HyShot II combustor at equivalence ratios slightly above 0.5 to be associated with boundary-layer separation. Based on this assumption, they used their results to test the validity of the boundary-layer separation criterion proposed by Korkegi (1975). This criterion was derived from measurements of shock-induced boundary-layer separation, but Frost *et al.* (2009) concluded that it is also appropriate for the more gradual pressure increases encountered in supersonic combusting flows. Thermal choking was ruled out as the cause of the choking behaviour based on a simple Rayleigh-type flow analysis. A similar analysis in § 4.2 of the present work also led to the conclusion that the onset of boundary-layer separation should precede that of thermal choking.

However, in both the experiments and the unsteady numerical simulation at $\phi = 0.6$ – 0.7 in the present work, we have seen that the transient flow and combustion features that develop within the combustion chamber at the onset of choking are consistent with thermal choking, rather than boundary-layer separation, being the responsible mechanism. Although the experiments were less extensive at $\phi = 0.5$, and the findings thus less conclusive, the results obtained suggested the same mechanism to be responsible as in the higher- ϕ case; this was confirmed by the corresponding numerical simulation. The immediate implication is that, although boundary-layer separation may have occurred at some point during the choking development in the experiments of Frost *et al.* (2009), their assumption that it was the driving mechanism is likely to be in error. The conclusion of these authors regarding the validity of the Korkegi criterion is therefore also questionable.

A more important conclusion from the present results concerns the nature of thermal choking in scramjet combustors and the apparent inability of a simple Rayleigh-type analysis to provide an adequate quantitative prediction for the onset of thermal choking. We attribute this to the one-dimensional approximation of the

Rayleigh analysis, whereby the flow conditions are assumed to be uniform across the duct. The present numerical simulations have shown that, contrary to this assumption, the combustion-related heat release occurs principally over a relatively limited cross-sectional area of the flow, centred around the shear layer between the incoming air stream and the injected hydrogen. Thus, the reduction in Mach number over the stream tube that covers this main combustion region may be significantly larger than that which would result from uniform heat release across the entire duct, leading to an earlier onset of thermal choking. If such ‘local’ thermal choking occurs, however, the possibility remains for the flow field to adjust itself through the generation of upstream-propagating disturbances, resulting in a modified flow configuration in which the heat release is redistributed away from the choked stream tube(s). Thus, new steady or quasi-steady flow topologies may arise in constant-area ducts, without the full inlet unstart that will almost always result if the global thermal choking limit is reached. (New topologies may be possible in the latter case if, for example, the overall combustion efficiency is reduced or the injector flow is affected; these possibilities cannot be completely ruled out but appear unlikely to occur in practice.) Such quasi-steady topologies were observed in the present work, in both the $\phi \approx 0.66$ experiments and the $\phi = 0.55$ computation.

That the localized nature of the heat release in scramjet engines could lead to a significant drop in the local Mach number was recognized as early as Ferri (1968). Nevertheless he saw no problem with the flow passing smoothly from supersonic to subsonic conditions, and suggested that this would lead to an embedded region of reversed flow, rather than the unsteady choking behaviour observed here. The possibility of such a deceleration in one-dimensional flows, given the right combination of changes in area, stagnation temperature and frictional length, was also noted by Shapiro (1953). The latter writes, however (p. 236): ‘the continuous transition from supersonic to subsonic speeds ... is hardly ever realized in practice, and is probably unstable under most conditions’.

8. Simplified theoretical analysis

8.1. Rayleigh flow with moving shock

In order to gain a better understanding of the shock-propagation behaviour observed in the experiments and computations described thus far, a simple one-dimensional quasi-unsteady analysis was performed. Although it was concluded in the previous section that such one-dimensional analyses fail to predict adequately, for example, the onset of thermal choking in complex three-dimensional flows, they can nevertheless provide valuable insights into the qualitative nature of the phenomena encountered. The present analysis is based on conventional steady Rayleigh flow, i.e. stagnation temperature change through heat addition in a constant-area duct, but includes a moving normal shock within the flow domain. It is a well-known property of Rayleigh flow that, whether the initial Mach number is subsonic or supersonic, heat addition drives the flow towards sonic conditions, and once this sonic state is reached, no further heat addition is possible without a modification to the inflow conditions. It is precisely such excess heat addition that was determined to give rise to the choking behaviour in the present study.

The situation just described is not altered by the introduction of a stationary normal shock into the flow, since the stagnation temperature is constant through such a shock. If the shock position is unsteady, however, the picture changes. This is because, in a frame of reference in which the shock is moving, neither the stagnation

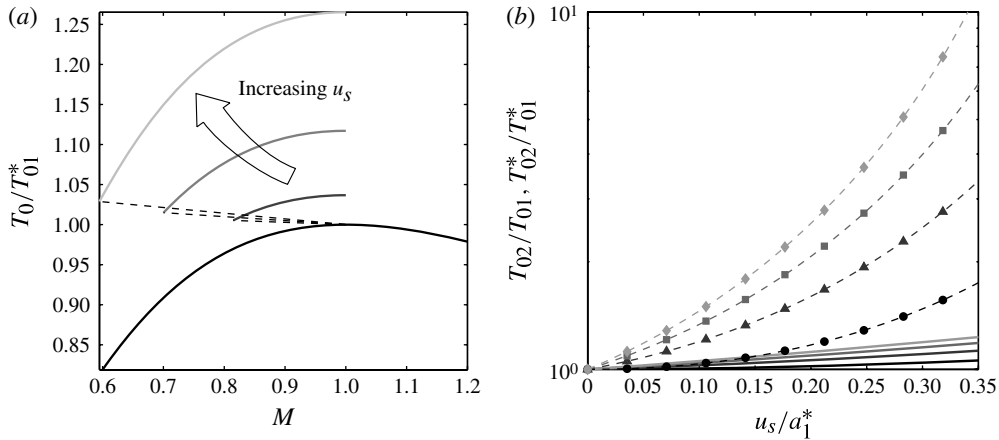


FIGURE 18. (a) Curves of stagnation temperature versus Mach number assuming conventional Rayleigh flow (base curve) and Rayleigh flow following an upstream-propagating normal shock of speed u_s , inserted at the original Rayleigh-flow choking point. (b) Stagnation temperature ratios, T_{02}/T_{01} (solid lines), and choking stagnation temperature ratios, T_{02}^*/T_{01}^* (dashed lines/symbols), through an upstream-propagating normal shock with normalized speed u_s/a_1^* (the T_{02}^*/T_{01}^* curves assume choking through Rayleigh flow on either side of the shock). The four curves in each case are for pre-shock Mach numbers of 1.0 (●, darkest), 1.5 (▲), 2.0 (■) and 2.5 (◆, lightest).

temperature nor the choking stagnation temperature (assuming conventional Rayleigh flow otherwise) is constant across the shock. This is demonstrated in figure 18. In figure 18(a), curves of the stagnation temperature T_0 (normalized by the pre-shock choking stagnation temperature T_{01}^*) are plotted against the flow Mach number M for constant-area frictionless flow. The base curve (darkest) shows the standard Rayleigh relation, with $T_0/T_{01}^* = 1$ at $M = 1$. A stationary normal shock inserted at any point on the supersonic branch of this curve will simply shift the flow state horizontally to the subsonic branch, without any change to either T_0 or the choking stagnation temperature T_0^* . If the shock is moving, however, the post-shock state no longer lies on this curve. To see this, we introduce shocks with various upstream propagation speeds, u_s , at the Rayleigh choking point, $M = 1$ (we make this particular choice since it is the incipient shock formation point). The pre- and post-shock states for three such shocks of increasing strength are joined by dashed lines on figure 18(a). For each of these, the subsonic branch of the new Rayleigh curve starting from the post-shock state is also shown. There is a small stagnation temperature rise through each moving shock, but much more significant is the rise in choking stagnation temperature, i.e. T_0/T_{01}^* at $M = 1$. In effect, the propagating shock gives the flow more ‘room’ for heat to be subsequently added before choking occurs, resolving the inability of the steady flow to accept further heat addition.

This effect is demonstrated quantitatively in figure 18(b). Here, both the stagnation temperature ratio, T_{02}/T_{01} , and the choking stagnation temperature ratio, T_{02}^*/T_{01}^* , across the shock are plotted as functions of the normalized shock speed in the laboratory frame, u_s/a_1^* , where a_1^* is the Rayleigh-flow choking sound speed at pre-shock conditions. The subscripts 1 and 2 refer here to pre- and post-shock conditions, respectively. Results for pre-shock Mach numbers of $M_1 = 1, 1.5, 2$ and 2.5 are shown; a ratio of specific heats of $\gamma = 1.4$ is assumed in all cases. Monotonic

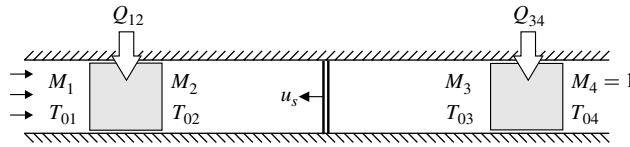


FIGURE 19. Simplified model of heat release and quasi-unsteady shock propagation in a constant-area combustion chamber.

increases in T_{02}/T_{01} and T_{02}^*/T_{01}^* with both u_s/a_1^* and M_1 are observed. Both T_{02}/T_{01} and T_{02}^*/T_{01}^* are always greater than unity for $u_s > 0$ (i.e. upstream shock propagation), but the rise in stagnation temperature is negligible in comparison to that in the choking stagnation temperature. In fact, the moving shock provides a mechanism that would allow potentially infinite energy to be added to the flow before choking occurs, since $T_{02}^*/T_{01}^* \rightarrow \infty$ as we tend to the limit of a zero post-shock flow velocity in the laboratory frame of reference.

8.2. Quasi-unsteady Rayleigh-flow model of choking scramjet combustor

To determine the implications of this behaviour for the supersonic combustion configuration under investigation in the present work, we construct a simplified one-dimensional model as shown in figure 19. Two regions of conventional Rayleigh flow, with total heat additions of Q_{12} and Q_{34} , respectively, are separated by a normal shock moving up the duct at a constant speed, u_s (the use of the term ‘quasi-unsteady’ to describe the model refers to the stipulation that u_s is constant). The flow is assumed to be thermally choked after the second region of Rayleigh flow (i.e. $M_4 = 1$); it is precisely this choking that drives the shock motion upstream. This assumption is similar to the Chapman–Jouget (CJ) condition for a detonation wave, except that the sonic condition is applied in the laboratory frame rather than in one moving with the shock. In general, this will result in a lower shock-propagation speed than the CJ condition, since M_3 will be smaller than the post-shock Mach number in the shock frame by an amount u_s/a_3 ; thus, a larger Q_{34} will be required to reach sonic conditions.

There are several major approximations inherent to this model. First, frictional and mass-addition effects are ignored, as are any changes to the physical properties of the gases due to combustion. Furthermore, for the shock speed to be constant, we must assume that Q_{12} and Q_{34} have been unchanging for sufficient time that the downstream choking location has been able to communicate with the shock and establish a quasi-unsteady configuration. Thus, either the shock-propagation speed must be small or the heat-addition regions must be physically separated from the shock. More formally, a condition such as $u_s(dQ/dx)/Q_{tot} \ll \bar{a}/(2d)$ can be specified, where $Q_{tot} = Q_{12} + Q_{34}$, d is the distance between the shock and the choking location, \bar{a} is the mean sound speed in this region, and dQ/dx is evaluated at the shock location. This assumption will become increasingly approximate as the shock approaches the injection location, as the streamwise derivative of the heat release is typically greatest there (Curran *et al.* 1996). It is further assumed that the coupling between the shock propagation and the downstream heat release region is in the laboratory frame. An example where this is not the case is a detonation wave, where the coupling is in the shock frame. Finally, we assume a single normal shock, rather than the shock train observed in experiments and computations. Considering a control volume around a shock train and assuming both that viscous losses are negligible and that conditions across the inlet and exit

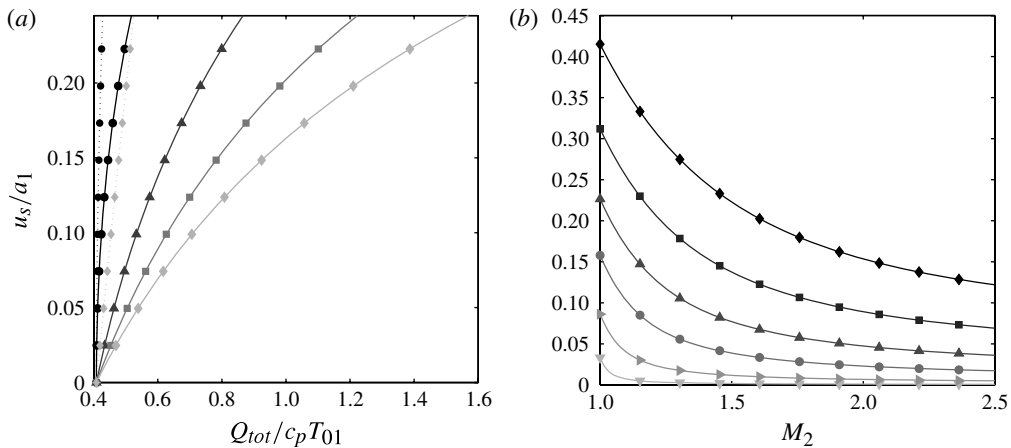


FIGURE 20. (a) Curves of the normalized shock speed, u_s/a_1 , versus the normalized total heat release for the simplified quasi-unsteady Rayleigh model shown in figure 19, assuming $M_1 = 2.5$ and for pre-shock Mach numbers of $M_2 = 1.0$ (●), 1.5 (▲), 2.0 (■) and 2.5 (◆). The dotted curves show the equivalent Chapman–Jouget detonation wave speeds for $M_2 = 1.0$ and 2.5 . (b) Curves of u_s/a_1 versus M_2 for $Q_{tot}/c_p T_{01} = 0.41$ (▼), 0.42 (►), 0.45 (●), 0.5 (▲), 0.6 (■) and 0.8 (◆).

planes of the control volume are uniform, the resulting conservation equations are exactly the same as for a single normal shock (Heiser & Pratt 1994), and thus so are the post-shock properties. For an extended shock train, however, the earlier assumption that the ‘shock’ is physically separated from the heat-addition regions becomes less tenable. In light of these points (as well as the considerable approximation inherent in the one-dimensional assumption), we employ the model here only to provide insight into the qualitative behaviour of the choking shock motion, rather than to make quantitative predictions of the shock speed.

In order to maintain consistency with the entrance conditions of the combustion chamber in the present investigation, we assume an initial Mach number, M_1 , of 2.5. The shock speed is then uniquely determined by the chosen values of $Q_{12}/c_p T_{01}$ and $Q_{34}/c_p T_{01}$, through the Rayleigh-flow and normal-shock relations. In figure 20(a) we show the normalized shock speed, u_s/a_1 , as a function of the total heat addition, $Q_{tot}/c_p T_{01} = (Q_{12} + Q_{34})/c_p T_{01}$, for different distributions of Q_{tot} between Q_{12} and Q_{34} . Four curves for choices of Q_{12} such that $M_2 = 1.0, 1.5, 2.0$ and 2.5 are plotted. The value of M_2 can be roughly correlated with the position of the shock within the combustor: $M_2 = 1$ corresponds to the location at which the incipient shock forms, and $M_2 = M_1 = 2.5$ to shock propagation upstream of injection. For the present choice of M_1 , the minimum heat addition for the formation of an unsteady shock is $Q_{tot}/c_p T_{01} = 0.409$; from this value, the shock speed rises monotonically with increasing total energy addition for all M_2 . For $M_2 = 1$, the shock speed rises extremely rapidly, the slope of the curve being infinite at the incipient shock formation point. Thus, the initial shock speed is very sensitive to the total heat addition, which may explain to some extent the disagreement between the experimental and computational shock speeds in §5. The normalized experimental shock speed for $\phi = 0.66$, for example, is $u_s/a_1 = 0.13$, which corresponds to $Q_{tot}/c_p T_{01} = 0.44$ for $M_2 = 1$; this compares to $u_s/a_1 = 0.26$ and $Q_{tot}/c_p T_{01} = 0.53$ for the $\phi = 0.715$

numerical result. This sensitivity may be understood physically to arise from the choice of the laboratory frame of reference in determining the shock speed: in the more natural frame fixed to the flow, the discrepancy in u_s/a_1 is reduced from 100% to approximately 8%.

A further observation is that, for a given $Q_{tot}/c_p T_{01}$, the shock speed slows as the Mach number ahead of the shock, M_2 , increases. This is shown more clearly in figure 20(b), in which u_s/a_1 is plotted against M_2 for several values of $Q_{tot}/c_p T_{01}$ between 0.41 and 0.8. Hence, we would expect a decrease in the propagation speed as the shock propagates up the duct, which is consistent with the experimental behaviour depicted in figure 8 and the numerical result for $\phi = 0.55$. That no notable slowing was observed in the $\phi = 0.7$ simulation is probably related to the accelerated flow development, meaning that the choking location did not have sufficient time to communicate with the moving shock and retard its progress as it moved upstream.

Also shown in figure 20(a) are corresponding curves for the CJ detonation wave speeds with $M_2 = 1.0$ and 2.5; here, Q_{34} is equated with the enthalpy change across the detonation wave. As predicted earlier, the detonation wave speeds are significantly higher than the equivalent choking shock speeds. Again, an extremely rapid increase of u_s/a_1 with $Q_{tot}/c_p T_{01}$ (even more so than in the corresponding choking shock curve) is observed for $M_2 = 1.0$.

Employing different values of the initial Mach number, M_1 , results in similar curves to those shown in figure 20. A higher M_1 shifts the choking limit of $Q_{tot}/c_p T_{01}$ to a larger value, but the qualitative trends remain identical.

8.3. Comparison of thermal and area-contraction choking

As noted in § 1, a common practice to reproduce scramjet-like choking behaviour in non-combusting flows is to employ mechanical throttling, i.e. introducing a flow obstruction to simulate the combustion-induced pressure rise. If the resulting area reduction is sufficient to produce a physically choked throat, such throttling could conceivably be employed to simulate unsteady thermal choking processes. The simplified model developed in the previous subsection provides a convenient means to compare the unsteady behaviour in the two cases (physical and thermal choking), and, in particular, to estimate the range of heat-release conditions that mechanical throttling can reproduce, based on the criterion of equal shock speeds. For physical choking, we assume a situation similar to that shown in figure 19, but with the first heat-release region (Q_{12}) removed and the second (Q_{34}) replaced by an isentropic compression with a minimum area ratio A^*/A at x^* . For a given M_1 , and assuming that the back-pressure is sufficiently low that a sonic throat forms at x^* , the shock speed is uniquely determined by the value of A^*/A . To match this shock speed with that produced by thermal choking, we must choose particular values of Q_{12}/Q_{tot} , or alternatively M_2 . Two values are of special interest: $M_2 = 1$, corresponding to the onset of the unsteady choking behaviour; and $M_2 = M_1$ (i.e. $Q_{12} = 0$), corresponding to the propagation of the shock (system) ahead of the injection point (i.e. in the isolator). This latter choice is typically regarded as the phase of the unsteady flow development that mechanical throttling is most suitable for simulating.

Before proceeding to discuss the relevant results, a key difference between physical and thermal choking in this context should be noted. The total heat release necessary to induce thermal choking is not affected by the introduction of a stationary normal shock, as the stagnation temperature is thereby unchanged. In contrast, except for the trivial case of initially sonic flow, the isentropic area-contraction ratio necessary to induce physical choking is so altered, with the critical area ratio for the onset

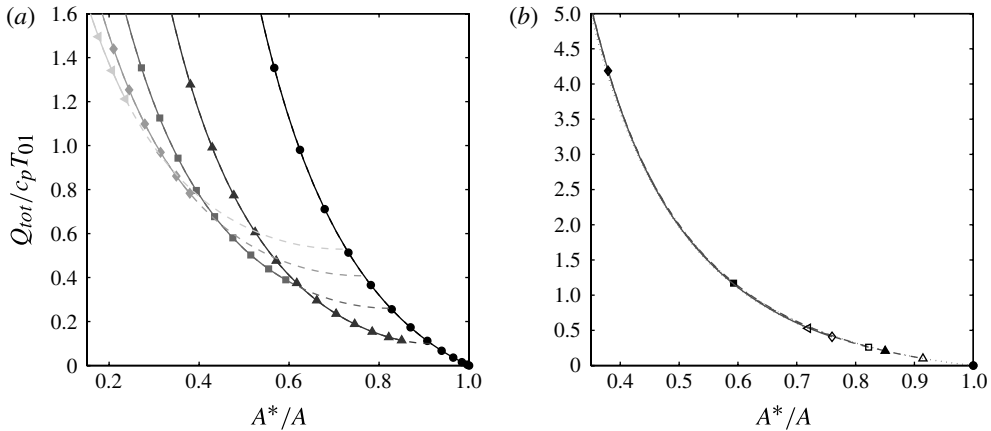


FIGURE 21. A comparison of the thermal and area-contraction choking characteristics required to produce equivalent quasi-unsteady flows. The total heat addition is plotted against the choking area ratio producing the same shock-propagation speed, assuming (a) $M_2 = 1$ and (b) $M_2 = M_1$ in the thermal choking model. The initial Mach numbers are $M_1 = 1.0$ ($\cdots \circ \cdots$), 1.5 ($-\cdots \triangle -\cdots$), 2.0 ($--- \square ---$), 2.5 ($-\diamond-$) and 3.0 ($\cdots \triangleleft \cdots$). In the left plot, the dashed part of the curve indicates area ratios between $(A^*/A)_{sub}$ and $(A^*/A)_{super}$; in the right plot, these two points for each curve are indicated by open and closed symbols, respectively.

of choking from post-shock (i.e. subsonic) conditions, $(A^*/A)_{sub}$, invariably larger than that from pre-shock (supersonic) conditions, $(A^*/A)_{super}$. Thus, if we start with a configuration in which $A^*/A = 1$ and steadily decrease A^*/A (while keeping the compression isentropic), the flow will remain shock-free until $(A^*/A)_{super}$ is reached, at which point a shock will form and immediately begin to travel upstream. If A^*/A is subsequently increased during the shock propagation, this will be communicated to the shock via expansion waves, reducing the propagation speed until the shock becomes stationary at $(A^*/A)_{sub}$. Further increases in A^*/A will unchoke the duct. Thus, in this idealized case of isentropic area-contraction choking, a hysteresis in the shock-propagation behaviour will occur; a similar effect has been used in the starting of variable-geometry supersonic inlets (Shapiro 1953). No such behaviour will be exhibited for thermal choking. In reality, however, the supersonic contraction is unlikely to be isentropic, and the formation of oblique shocks with resulting shock–boundary-layer interactions will promote the onset of boundary-layer separation, which may itself trigger choking before $(A^*/A)_{super}$ is reached.

Returning now to specific results, in figure 21(a) we show curves of the area ratios required to reproduce the same shock speed as heat releases of $Q_{tot}/c_p T_{01}$, assuming $M_2 = 1$, for five initial Mach numbers between 1 and 3. In light of the discussion in the previous paragraph, all but the $M_1 = 1$ curve are divided into two parts: the left branches (solid lines and symbols) correspond to area ratios below $(A^*/A)_{super}$, whereas the right branches (dashed lines) cover area ratios between $(A^*/A)_{super}$ and $(A^*/A)_{sub}$. The left branch of each curve thus represents conditions that are achievable through a one-way isentropic reduction in A^*/A . As the initial Mach number is increased, the minimum value of $Q_{tot}/c_p T_{01}$ for choking becomes larger, and both $(A^*/A)_{super}$ and $(A^*/A)_{sub}$ show corresponding reductions. The value of $(A^*/A)_{super}$ is affected more strongly, which leads to a growing difference between the values of $Q_{tot}/c_p T_{01}$ at the two choking area ratios. For $M_1 = 2.5$, for example, the

heat release corresponding to $(A^*/A)_{super}$, $Q_{tot}/c_p T_{01} \approx 0.75$, is almost double that at $(A^*/A)_{sub}$. Referring to the $M_2 = 1$ curve in figure 20, we see that heat release values of this magnitude would produce shock speeds well in excess of those observed in practice, suggesting that it becomes increasingly difficult for area-contraction choking to reproduce relevant thermal choking behaviour as the initial Mach number is increased much above unity.

Similar curves are shown in figure 21(b) for $M_2 = M_1$. In this case, the curves for the different initial Mach numbers lie very close to one another. For clarity, we thus plot $(A^*/A)_{sub}$ and $(A^*/A)_{super}$ for each Mach number using open and closed versions, respectively, of the same symbol. Similar comments apply here as in figure 21(a), but we note the significantly larger values of $Q_{tot}/c_p T_{01}$ corresponding to $(A^*/A)_{super}$. This is especially the case for the higher Mach numbers considered: for $M_1 = 3.0$, the relevant point lies well off the plotted scale. Thus, even for studying transient choking phenomena in isolators, mechanical throttling appears limited to shock-propagation behaviour dominated by flow separation. This conclusion is consistent with the experimental findings of Wagner *et al.* (2009), for example.

9. Conclusions

A series of experiments has been carried out in the HEG shock-tunnel facility to investigate the transient fluid-combustion phenomena that develop in the HyShot II combustor under high-equivalence-ratio conditions. In addition to surface pressure measurements on the injector and cowl-side walls, high-speed flow visualization in the form of pulsed diode laser schlieren and OH* chemiluminescence was employed. Schlieren images revealed that the unstart process begins with the formation of a shock train in the central to rear combustion chamber that subsequently propagates upstream. Although both the location of the onset of this shock train and its speed of propagation were found to depend strongly on the equivalence ratio, the physical nature of the system appeared similar in all cases. OH* visualizations did not indicate the presence of strong separation features propagating upstream with the shock train near its point of formation, suggesting that the driving mechanism for the transient development was thermal choking. Nevertheless, boundary-layer separation was observed to develop on the injector-side wall when the shock train had moved further upstream.

Unsteady numerical simulations of the experimental configuration were performed using the DLR TAU code. These confirmed the main qualitative findings from the experiments, revealing localized boundary-layer separation to develop at some point during the propagation of the shock train, but not to be the mechanism responsible for its initial formation. The computations also indicated that the global choking behaviour was dictated by the limited region of maximum heat release at the shear layer between the incoming air stream and the injected hydrogen. This led to the concept of ‘local’ thermal choking and suggested that integral estimates based on one-dimensional assumptions give unreliable quantitative predictions for the onset of thermal choking. Further, such localized choking can result in the development of new quasi-steady flow topologies, as observed in both the $\phi \approx 0.66$ experiments and the $\phi = 0.55$ numerical simulation.

Following full inlet unstart in the experiments, high-amplitude pressure oscillations were observed to develop in the combustion chamber. The frequency content of the measured signals was found to be consistent with a simple acoustic analysis.

A one-dimensional quasi-unsteady model based on Rayleigh flow was proposed to explain aspects of the transient shock-propagation behaviour. In particular, this model

predicts a slowing of the shock train as it moves upstream, a phenomenon that was observed experimentally. It also predicts the initial shock-propagation speed to be very sensitive to the total heat release, which may explain the large discrepancies that were obtained between experimental and numerical shock speeds. Finally, by constructing an equivalent model for area-contraction-based choking, the difficulty of employing mechanical throttling to simulate relevant thermal choking behaviour in scramjet combustion chambers and isolators was highlighted.

Acknowledgements

This work was performed within the ‘Long-Term Advanced Propulsion Concepts and Technologies II’ (LAPCAT II) project investigating high-speed transportation. LAPCAT II, coordinated by ESA-ESTEC under the supervision of J. Steelant, is supported by the EU within the Seventh Framework Program, Theme 7 TRANSPORT, Contract no. ACP7-GA-2008-21 1485. The authors wish to acknowledge the assistance of the HEG technical staff, in particular I. Schwendtke and M. Jünemann, in preparing the experiments, and M. Schmidt from the DLR design office in the design of the model.

REFERENCES

- BERTIN, J. J., STETSON, K. F., BOUSLOG, S. A. & CARAM, J. M. 1997 Effect of isolated roughness elements on boundary-layer transition for Shuttle Orbiter. *J. Spacecr. Rockets* **34** (4), 426–436.
- BOYCE, R. R., PAULL, A., STALKER, R. J., WENDT, M., CHINZEI, N. & MIYAJIMA, H. 2000 Comparison of supersonic combustion between impulse and vitiation-heated facilities. *J. Propul. Power* **16** (4), 709–717.
- CURRAN, E. T., HEISER, W. H. & PRATT, D. T. 1996 Fluid phenomena in scramjet combustion systems. *Annu. Rev. Fluid Mech.* **28**, 323–360.
- DO, H., IM, S., MUNGAL, M. G. & CAPPELLI, M. A. 2011 The influence of boundary layers on supersonic inlet flow unstart induced by mass injection. *Exp. Fluids* **51** (3), 679–691.
- FERRI, A. 1968 Review of SCRAMJET propulsion technology. *J. Aircraft* **5** (1), 3–10.
- FROST, M. A., GANGURDE, D. Y., PAULL, A. & MEE, D. J. 2009 Boundary-layer separation due to combustion-induced pressure rise in supersonic flow. *AIAA J.* **47** (4), 1050–1053.
- GARDNER, A. D., HANNEMANN, K., STEELANT, J. & PAULL, A. 2004 Ground testing of the Hyshot supersonic combustion flight experiment in HEG and comparison with flight data. *AIAA Paper* 2004-3345.
- GERHOLD, T., FRIEDRICH, O., EVANS, J. & GALLE, M. 1997 Calculation of complex three-dimensional configurations employing the DLR TAU code. *AIAA Paper* 97-0167.
- GERLINGER, P. 2001 An implicit multigrid method for turbulent combustion. *J. Comput. Phys.* **167**, 247–276.
- HABER, L. C. & VANDSBURGER, U. 2003 A global reaction model for OH* chemiluminescence applied to a laminar flat-flame burner. *Combust. Sci. Technol.* **175**, 1859–1891.
- HANNEMANN, K. 2003 High enthalpy flows in the HEG shock tunnel: experiment and numerical rebuilding. *AIAA Paper* 2003-978.
- HANNEMANN, K., KARL, S., SCHRAMM, J. M. & STEELANT, J. 2010 Methodology of a combined ground based testing and numerical modelling analysis of supersonic combustion flow paths. *Shock Waves* **20**, 353–366.
- HANNEMANN, K., SCHNIEDER, M., REIMANN, B. & SCHRAMM, J. M. 2000 The influence and delay of driver-gas contamination in HEG. *AIAA Paper* 2000-2593.
- HANNEMANN, K., SCHRAMM, J. M., KARL, S. & STEELANT, J. 2008 Experimental investigation of different scramjet hydrogen injection systems. In *Proceedings of the 6th European Symposium on Aerothermodynamics for Space Vehicles, Versailles, France*.

- HEISER, W. H. & PRATT, D. T. 1994 *Hypersonic Airbreathing Propulsion*. AIAA Education Series. AIAA.
- HERNING, F. & ZIPPERER, L. 1936 Beitrag zur Berechnung der Zähigkeit technischer Gasgemische aus den Zähigkeitswerten der Einzelbestandteile. *Gas- und Wasserfach* **4**, 69–73.
- JAMESON, A. 1991 Time dependent calculations using Multigrid, with application to unsteady flows past airfoils and wings. *AIAA Paper* 91-1596.
- KARL, S. 2011 Numerical investigation of a generic scramjet configuration. PhD thesis, Technische Universität Dresden, Germany.
- KARL, S. & HANNEMANN, K. 2008 CFD analysis of the HyShot II scramjet experiments in the HEG shock tunnel. *AIAA Paper* 2008-2548.
- KORKEGI, R. H. 1975 Comparison of shock induced two- and three-dimensional incipient turbulent separation. *AIAA J.* **13** (4), 534–535.
- KREK, R. M. & JACOBS, P. A. 1993 STN, shock tube and nozzle calculations for equilibrium air. *Rep. 2/93*. Department of Mechanical Engineering, University of Queensland.
- LOVE, E. S. 1955 Pressure rise associated with shock-induced boundary-layer separation. NACA Tech. Note NACA-TN-3601.
- MATSUO, K., MIYAZATO, Y. & KIM, H.-D. 1999 Shock train and pseudo-shock phenomena in internal gas flows. *Prog. Aerosp. Sci.* **35**, 33–100.
- MCDANIEL, K. S. & EDWARDS, J. R. 1999 Simulation of thermal choking in a model scramjet combustor. *AIAA Paper* 99-3411.
- MCDANIEL, K. S. & EDWARDS, J. R. 2001 Three-dimensional simulation of thermal choking in a model scramjet combustor. *AIAA Paper* 2001-0382.
- MUSIELAK, D. 2011 Year in review: high-speed air-breathing propulsion. *Aerospace America*, December, p. 49.
- NEWSOME, R. W. 1984 Numerical simulation of near-critical and unsteady, subcritical inlet flow. *AIAA J.* **22** (10), 1375–1379.
- O'BYRNE, S., DOOLAN, M., OLSEN, S. R. & HOUWING, A. F. P. 2000 Transient thermal choking processes in a model scramjet engine. *J. Propul. Power* **16** (5), 808–814.
- PAULL, A., ALESI, H. & ANDERSON, S. M. 2003 The methodology behind the HyShot flight program. In *Proceedings of the 10th Australian International Aerospace Congress and 14th National Space Engineering Symposium, Brisbane, Australia*.
- RODI, P. E., EMAMI, S. & TREXLER, C. A. 1996 Unsteady pressure behaviour in a ramjet/scramjet inlet. *J. Propul. Power* **12** (3), 486–493.
- SETTLES, G. S. 2006 *Schlieren and Shadowgraph Techniques*. Springer.
- SHAPIRO, A. H. 1953 *The Dynamics and Thermodynamics of Compressible Fluid Flow*. Ronald Press.
- SHIMURA, T., MITANI, T., SAKURANAKA, N. & IZUMIKAWA, M. 1998 Load oscillations caused by unstart of hypersonic wind tunnels and engines. *J. Propul. Power* **14** (3), 348–353.
- SMART, M. K., HASS, N. E. & PAULL, A. 2006 Flight data analysis of the HyShot 2 scramjet flight experiment. *AIAA J.* **44** (10), 2366–2375.
- SUNAMI, T., ITOH, K., SATO, K. & KOMURO, T. 2006 Mach 8 ground tests of the hypermixer scramjet for HyShot-IV flight experiment. *AIAA Paper* 2006-8062.
- SUNAMI, T. & KODERA, M. 2012 Numerical investigation of a detonation wave system in a scramjet combustor. *AIAA Paper* 2012-5861.
- TAN, H.-J. & GUO, R. W. 2007 Experimental study of the unstable-unstarted condition of a hypersonic inlet at Mach 6. *J. Propul. Power* **23** (4), 783–788.
- TAN, H.-J., LI, L. G., WEN, Y.-F. & ZHANG, Q.-F. 2011 Experimental investigation of the unstart process of a generic hypersonic inlet. *AIAA J.* **49** (2), 279–288.
- WAGNER, J. L., YUCEIL, K. B., VALDIVIA, A., CLEMENS, N. T. & DOLLING, D. S. 2009 Experimental investigation of unstart in an inlet/isolator model in Mach 5 flow. *AIAA J.* **47** (6), 1528–1542.
- WIETING, A. R. 1976 Exploratory study of transient unstart phenomena in a three-dimensional fixed-geometry scramjet engine. NASA Tech. Note TN D-8156.
- WILKE, C. R. 1950 A viscosity equation for gas mixtures. *J. Chem. Phys.* **18** (4), 517–519.